TECHNISCHE UNIVERSITÄT WIEN

Diplomarbeit

Mid-Infrared Plasmonic Waveguide Design and Characterization for a Chip-Scale Heterodyne Receiver

zur Erlangung des akademischen Grades

Diplom-Ingenieur

im Rahmen des Studiums

Physikalische Energie- und Messtechnik

(066 460)

eingereicht von

Xaver Gsodam
Matrikelnummer 11702812

ausgeführt am Institut für Festkörperelektronik
der Fakultät für Elektrotechnik und Informationstechnik der Technischen Universität Wien

Betreuung
Betreuer: Univ.Prof. i.R. Mag.rer.nat. Dr.rer.nat. Gottfried Strasser
und Dr. sc. Borislav Hinkov
Mitwirkung: , M.Sc. Mauro David, M.Sc. Georg Marschick, BSc Dominik Koukola

Wien, 19.09.2023

(Unterschrift Verfasser) (Unterschrift Betreuer)

Kurzfassung

Das rasche Voranschreiten datenintensiver Technologien wird in naher Zukunft Lösungen für kabellosen Datentransfer bei hohen Übertragungsraten erfordern. Optische Freiraumkommunikation (FSO) mittleren Infrarotspektrum bietet eine solche Lösung. Diese Arbeit trägt zum Design und Optimierung eines on-chip heterodynen Empfängers mit Funktionsbereich im atmosphärischen Fenster des langwelligen Infrarots ($8-12\ \mu m$). Signalverstärker, lokaler Oszillator und Photodetektor bestehen alle aus demselben Quantenkaskaden-Material. Das Hauptaugenmerk dieser Arbeit liegt jedoch auf den Germanium-basierten plasmonischen Wellenleitern welche als Strahlvereiniger am on-chip heterodynen Empfänger fungieren, wobei die Minimierung von Verlusten von größter Wichtigkeit ist. Mit Simulationen, durchgeführt mit der Software *COMSOL Multiphysics*, werden zwei Wellenleiterdesigns miteinander verglichen. Das erste design, eine schmale aber hohe Geometrie ($1 \times 2\ \mu m$), zeigt die Fähigkeit Oberflächenplasmonen selbst bei kleinen Kurvenradien lenken zu können, jedoch bei hohen Verlusten ($110\ dB/mm$). Im Gegensatz dazu weist das zweite design, eine breite aber flache Geometrie ($6 \times 0.3\ \mu m$), deutlich geringere Verluste auf ($16\ dB/mm$), ist aber nicht in der Lage die Ausbreitungsrichtung von Oberflächenplasmonen zu ändern. Um die Vorteile der flachen Geometrie nutzen zu können werden auf dem Chip integrierte goldüberzogene Mikrospiegelstrukturen zur Umlenkung von Oberflächenplasmonen als innovative Lösung angewendet. Aus den Resultaten der Simulationen lässt sich schließen, dass das hohe Wellenleiterdesign bis zu einer Länge von $47\ \mu m$ die geringeren Verluste aufweist. Experimente mit hergestellten Strukturen beweisen, dass das Spiegelkonzept auch praktisch anwendbar ist. Allerdings sind die den Spiegeln zugeordneten Verluste um etwa $5\ dB$ höher als die von den Simulationen vorhergesagten $2.2\ dB$. Die on-chip Charakterisierung der flachen Wellenleiter ergibt Verluste von

18.3 *dB*/*mm* und stimmt damit gut mit den Simulationen überein, während sich die derzeitige Fabrikationsmethode für die hohen Wellenleiter noch als unzuverlässig erweist. Weitere Experimente zeigen, dass im Wellenlängenbereich von $8065 - 8400$ *nm* die Verstärkung durch den Signalverstärker bis zu 10 *dB* erreicht. Abschließend identifiziert die Studie wichtige Verbesserungen für das zukünftige Design der Quantenkaskadenlaser und Quantenkaskadendetektoren.

Abstract

Rapid advancements in data-demanding technologies soon will necessitate high-speed wireless data transfer solutions. Free Space Optical (FSO) communication, operating in the mid-infrared range, offers a solution. This work contributes to the design and optimization of an on-chip heterodyne receiver operating in the long-wave infrared atmospheric window ($8 - 12$ μm). Signal amplifier, local oscillator, and photodetector are all based on the same quantum cascade material. The main focus of this work though lies on the Germanium-based plasmonic waveguides envisioned for beam combining within the on-chip heterodyne receiver, where minimizing losses is paramount. Simulations employing *COMSOL Multiphysics* software compare two waveguide designs. A narrow and thick geometry (1×2 μm), exhibits the ability to redirect the propagating surface plasmon polariton (SPP) even within tight bend radii but incurs high losses (110 *dB*/*mm*). In contrast a wide and thin waveguide geometry (6×0.3 μm), demonstrates significantly lower losses (16 *dB*/*mm*) but lacks SPP redirection capabilities. An innovative solution is found by introducing Au-covered micromirror structures directly implemented on the chip to redirect SPPs with the low loss geometry. Simulations show that the thick Ge Waveguide geometry excels in minimizing losses for waveguide lengths up to 47 μm. Experiments with fabricated devices prove that the mirror concept works, even though losses attributed to the mirrors are around 5 *dB* higher than the 2.2 *dB* predicted by simulations. On-chip waveguide characterization puts the losses of the thin Ge waveguides at 18.3 *dB*/*mm*, in good agreement with simulations, while the current fabrication method proved unreliable for the thick waveguides. Furthermore, optical gain from the optical amplifier reaches up to 10 *dB* within $8065 - 8400$ *nm*. Finally, the study identifies important improvements required for Quantum Cascade Laser and Quantum Cascade Detector design in future devices.

Contents

Abbreviations

BC bottom contact
BZ Brillouin zone
CB conduction band
DLSPPW dielectric-loaded surface plasmon polariton waveguide
EC-QCL external cavity quantum cascade laser
EMF electro magnetic field
EQE external quantum efficiency
FEM finite element method
FSO free optical space communication
IB interband
IF intermediate frequency
IQE internal quantum efficiency
ISB intersubband
LO local oscillator
LWIR long-wave infrared
MCT HgCdTe infrared photodetector
MDI metal-dielectric interface
PDM photodetector measurement
PL photolithography
QCD quantum cascade detector
QCL quantum cascade laser
QCLD quantum cascade laser and detector
QWIP quantum well infrared photodetector
RIE reactive ion-etch
RMS root mean square
SNR signal-to-noise ratio
SOA semiconductor optical amplifier
SPP surface plasmon polaritons
TC top contact
TE transverse electric
TM transverse magnetic
VB valence band
WG waveguide

1 Introduction

The rapid advancements in digitalization, remote control applications, autono- mous machinery, and various other areas present in our daily lives have generated an ever-growing demand for increased data transfer rates. While optical fibers have made high-speed data transmission in the *Gbit*/*s* range readily accessible on the ground, wireless technologies operating in the *GHz* frequency range face inherent limitations in keeping up with this escalating need [1]. A promising solution to this challenge is free space optical communication (FSO). This cutting-edge technology operates at optical frequencies, offering high bandwidth wireless data transmission through Earth's atmosphere and outer space. The numerous advantages of FSO include high-speed data rates up to the *Gbit*/*s* range, low latency, inherent security due to its resistance to interception, immunity to electromagnetic interference, and access to a broad spectrum without costly licensing restrictions [1–3]. Nonetheless, FSO faces a significant hurdle in the form of a high bit error rate, primarily caused by atmospheric impediments such as attenuation, turbulence, water vapor, and light-absorbing molecules in the air. Ensuring all-year-round reliable operation under diverse weather conditions necessitates the selection of frequencies within specific spectral regions known as "atmospheric windows." These are parts where atmospheric absorption is minimal. As shown in Figure 1.1 one such extensive atmospheric window exists in the long-wave infrared (LWIR) range, spanning from 8 to 12 μm. Recent advancements in quantum cascade technology have demonstrated remarkable achievements in FSO data transfer. Transmission rates reaching up to 11 *Gb*/*s*, at a wavelength of 9.7 μm were achieved, albeit over relatively short distances (25 *cm*) [4].

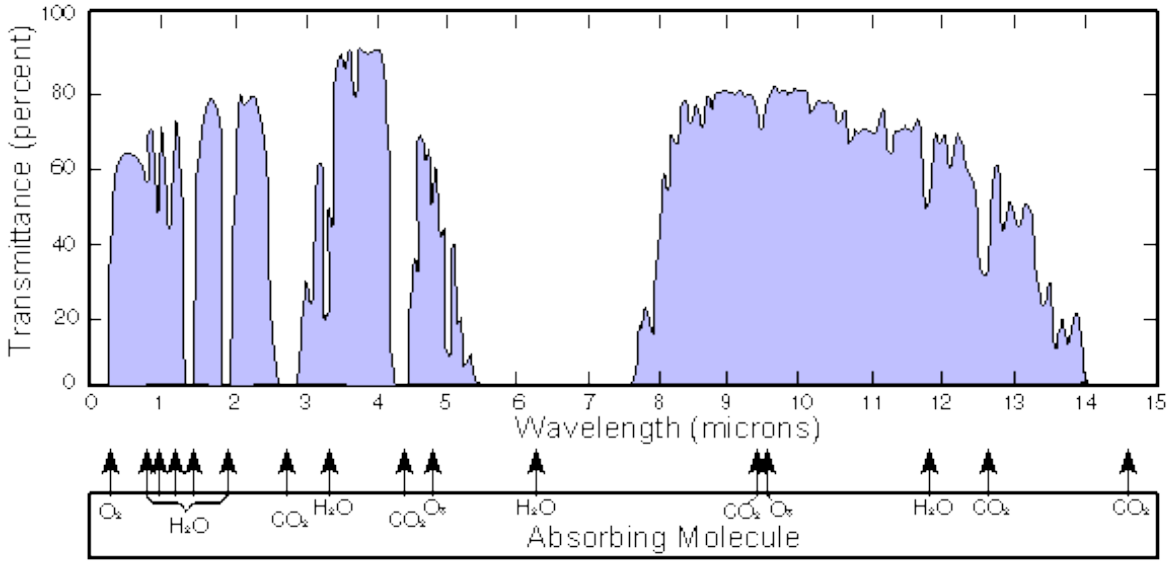

Figure 1.1: Atmospheric windows in the infrared. Image taken from [5].

The purpose of this work is to contribute to the design and optimization of an on-chip heterodyne receiver sensitive to radiation within the LWIR atmospheric window. The concept is based on a Quantum Cascade Material engineered for laser emission and photodetection at wavelengths within the range $8 - 8.5\ \mu m$. The main features of the heterodyne receiver are illustrated in Figure 1.2. The external signal is coupled and amplified through a semiconductor

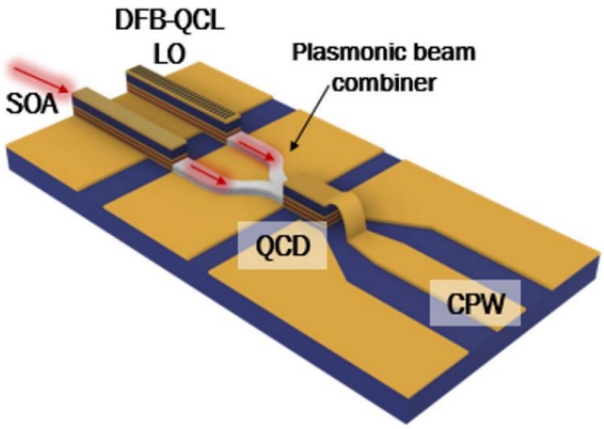

Figure 1.2: Heterodyne receiver based on quantum cascade laser and detector material with plasmonic beam combiner. Image taken from [6] with permission of the author.

optical amplifier (SOA). Subsequently, this signal is guided along a dielectric-loaded surface

plasmon polariton waveguide (DLSPPWG) structure, where it combines with the local oscillator (LO) signal. The resulting signal is then directed to the on-chip detector. The information carried by the input signal is extracted from the beating between the LO and external signal, significantly enhancing the signal-to-noise ratio (SNR). This research focuses on identifying suitable waveguide (WG) geometries for a Germanium beam combiner through simulations utilizing *COMSOL Multiphysics* software. Additionally, the project involves the characterization of fabricated WGs integrated into on-chip devices. Further, experiments to characterize quantum cascade lasers, detectors, and signal amplifiers are performed. The results serve as key indicators of the concept's potential and point out critical design issues requiring enhancement for optimal device performance.

2 Semiconductor Optical Waveguides

The well-established field of plasmonics studies collective oscillations of electrons, most commonly in metals at the interface with dielectric media. The first prediction of this physical phenomenon was made by Ritchie in 1957 [7]. The first experimental demonstration followed two years later by Stern and Ferrell [8]. In these early experiments, surface plasmons were excited by high-energy electrons, whereas in modern plasmonics electromagnetic fields (EMFs) are usually the source. Since then plasmonics conquered a large scientific domain, including applications in biosensing, microscopy, and subwavelength optics [9–11]. In plasmonic waveguides at optical frequencies, oscillations are excited by the electromagnetic field of incident light. Semiconductors such as Silicon and Germanium have proven to be useful waveguide materials in the mid-infrared due to their optical behavior within this domain [12]. In the following chapter the theory of plasmonics regarding surface plasmon polaritons (SPPs) and optical WGs operating with this concept are discussed.

2.1 Surface Plasmon Polaritons

2.1.1 The Drude Model

The collective oscillation of the free-electron gas at a metal-dielectric interface together with the electromagnetic oscillation inside the dielectric are often referred to as SPPs. The interaction between free electrons and a periodic EMF is described in this section with the classical Drude model following the equations in [13]. The equation of motion for a free electron in an

EMF with angular frequency ω is given by:

$$m_e \frac{d^2\vec{x}(t)}{dt^2} + m_e\gamma\frac{d\vec{x}(t)}{dt} = -|e|\vec{E}\exp(-i\omega t) \tag{2.1}$$

with the initial condition $\vec{x}(0) = 0$, the electron mass m_e, the dampening factor γ, the electron charge e and the electrical field inside the material $\vec{E}$. With the approach $\vec{x}(t) = \vec{A}\exp(-i\omega t)$, the amplitude of the electron's oscillation is:

$$\vec{A} = \frac{|e|\vec{E}}{m_e}\frac{1}{\omega^2 + i\gamma\omega} \tag{2.2}$$

The polarization in a medium is given by $\vec{P} = -n|e|\vec{x} = \varepsilon_0\chi\vec{E}$, where n is the material's electron density and χ is its electric susceptibility. The relative permittivity is then obtained by:

$$\varepsilon_r = 1 + \chi = 1 - \frac{\omega_p^2}{\omega(\omega + i\gamma)} \tag{2.3}$$

with the plasma frequency $\omega_p^2 = \frac{|e|^2 n}{\varepsilon_0 m_e}$. Here the effect of bound electrons is neglected. Splitting the permittivity into real and imaginary parts yields:

$$\begin{aligned} Re(\varepsilon) = \varepsilon' &= 1 - \frac{\omega_p^2}{\omega^2 + \gamma^2} \\ Im(\varepsilon) = \varepsilon'' &= \frac{\omega_p^2\gamma}{\omega^3 + \omega\gamma^2} \end{aligned} \tag{2.4}$$

They are related to the refractive index $\tilde{n} = n + i\kappa$ in the following way:

$$\begin{aligned} \varepsilon' &= n^2 - \kappa^2 \\ \varepsilon'' &= -2n\kappa \end{aligned} \tag{2.5}$$

The imaginary part κ relates to the attenuation of the material, while the real part n is the factor affecting wavelength and phase velocity of the EMWs inside the medium. Analyzing equations (2.4) and (2.5) one observes that at frequencies much lower than the plasma frequency ε' tends towards high negative values, while ε'' increases to high positive values. In this regime,

attenuation is high, which renders the material opaque to light in this frequency domain. In the other extreme of frequencies much higher than ω_p, ε'' rapidly approaches zero, while ε' approaches the value 1. At this limit, the material behaves optically like the vacuum and is, therefore, almost fully transparent. Figure 2.1 shows the real and imaginary components of the relative permittivity of Gold, which is well approximated by the Drude model.

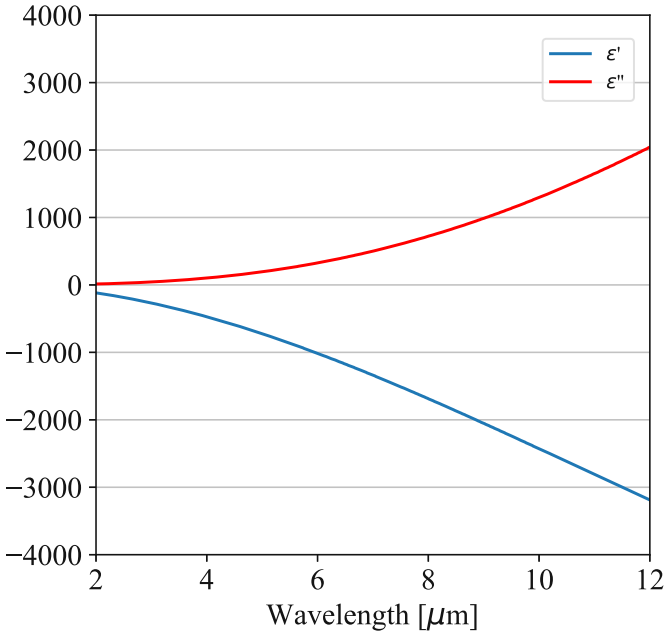

Figure 2.1: Real ε' and imaginary ε'' parts of the relative permittivity of 200 *nm* thick evaporated Gold on QCLD substrate. The data was obtained through ellipsometry measurements performed at the *Central European Institute of Technology* at Brno.

2.1.2 Maxwell's Equations

Due to their electromagnetic nature surface plasmons can be described with the fundamental Maxwell equations [14]:

$$\begin{aligned} \nabla \times \vec{E} &= -\frac{\partial \vec{B}}{\partial t} \\ \nabla \cdot \vec{B} &= 0 \\ \nabla \cdot \vec{D} &= \rho \\ \nabla \times \vec{H} &= \vec{j} + \frac{\partial \vec{D}}{\partial t} \end{aligned} \tag{2.6}$$

where $\vec{B}$ is the magnetic flux, $\vec{D}$ the electric displacement field, ρ the charge density, $\vec{H}$ the magnetic field and $\vec{j}$ the current density. The displacement field and the magnetic flux relate to the electric and magnetic fields via $\vec{D} = \varepsilon_0 \varepsilon_r \vec{E}$ and $\vec{B} = \mu_0 \mu_r \vec{H}$ respectively. μ_0 and μ_r denote the permeability in vacuum and the medium's relative permeability. By applying the curl operator on both sides of the first Maxwell equation and substituting the right-hand side with the identity from the fourth Maxwell equation one yields [14]:

$$-\Delta \vec{E} = -\mu_0 \mu_r \frac{\partial^2 \vec{D}}{\partial t^2} \tag{2.7}$$

in the absence of external currents and net charge densities. With $\vec{D} = \varepsilon_0 \varepsilon_r \vec{E}_{t=0} \exp(i\omega t)$, $\mu_r = 1$ and $\frac{1}{c_0} = \sqrt{\mu_0 \varepsilon_0}$ the expression can be rewritten as:

$$\Delta \vec{E} + \varepsilon k_0^2 \vec{E} = 0 \tag{2.8}$$

where $k_0 = \frac{\omega}{c_0}$ is the wavenumber of the EMW in vacuum. This equation is known as the Helmholtz equation and describes the dispersion relation of EMWs inside a medium under the mentioned conditions [14].

2.1.3 Dispersion of SPPs

It can be shown with the previous equations, that a transverse electric (TE) wave does not fulfill the continuity criteria at a metal-dielectric interface (MDI) [15]. Therefore, only the

transverse magnetic (TM) case ($\vec{H} = H\vec{e}_y$) is treated in the following. Figure2.2 illustrates the z-component of the electric field of a TM-polarized EMW, which continuously loses intensity as it propagates along the interface.

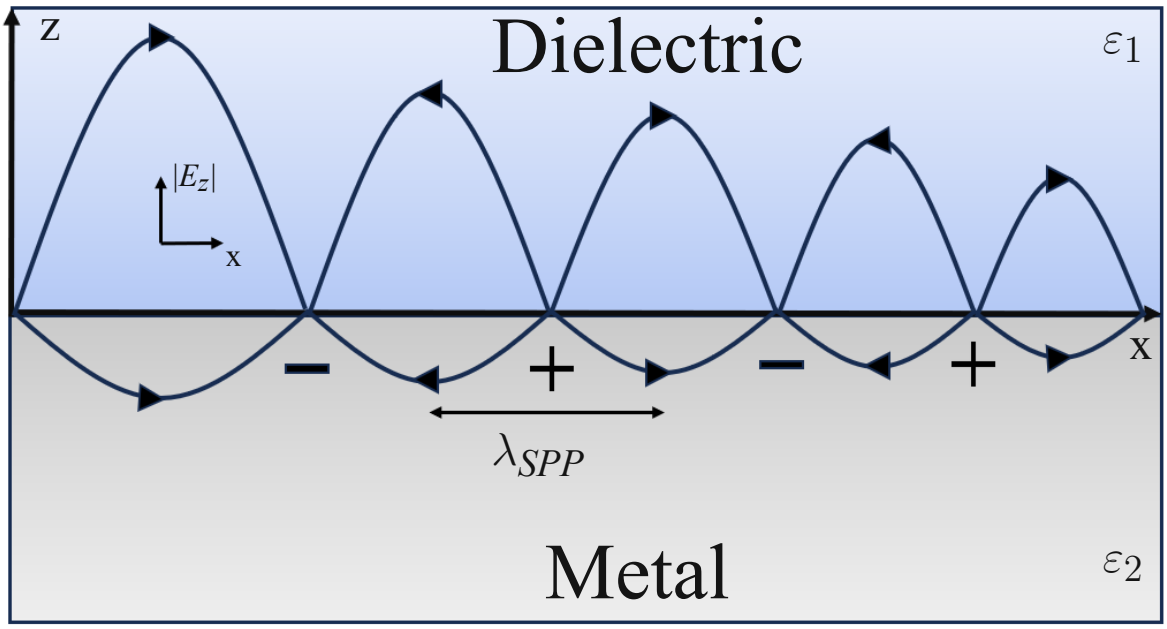

Figure 2.2: Surface plasmon polariton propagating in the x-direction along a metal-dielectric interface while decaying.

The component of the $\vec{H}$-Field and the resulting electric field components derived from the fourth Maxwell equation are given by [15]:

$$\begin{aligned} H_y &= H_d e^{i(\beta x - \omega t)} e^{-\alpha_d z} \\ E_x &= -\frac{i\alpha_d}{\omega \varepsilon_0 \varepsilon_d} H_d e^{i(\beta x - \omega t)} e^{-\alpha_d z} \\ E_z &= -\frac{\beta}{\omega \varepsilon_0 \varepsilon_d} H_d e^{i(\beta x - \omega t)} e^{-\alpha_d z} \end{aligned} \tag{2.9}$$

in the dielectric ($z \geq 0$) and

$$\begin{aligned} H_y &= H_m e^{i(\beta x - \omega t)} e^{\alpha_m z} \\ E_x &= \frac{i\alpha_m}{\omega \varepsilon_0 \varepsilon_m} H_m e^{i(\beta x - \omega t)} e^{\alpha_m z} \\ E_z &= -\frac{\beta}{\omega \varepsilon_0 \varepsilon_m} H_m e^{i(\beta x - \omega t)} e^{\alpha_m z} \end{aligned} \tag{2.10}$$

in the metal ($z \leq 0$). The propagation constant β denotes the x-component of the SPP wave vector. The α_i have positive real values and describe the exponential decay of the field as it extends into the media away from the surface. At the interface ($z = 0$) H_y, D_z and E_x have to be continuous. Therefore, $H_d = H_m$ and [15]

$$\frac{\alpha_d}{\alpha_m} = -\frac{\varepsilon_d}{\varepsilon_m} \tag{2.11}$$

As the α_i have positive values this equation leads to the condition $\varepsilon_m \varepsilon_d < 0$ required for the existence of surface plasmons in the case of nonmagnetic materials. The Helmholtz equation for the magnetic field leads to:

$$\Delta \vec{H} + \varepsilon k_0^2 \vec{H} = 0 \tag{2.12}$$

This results in the following conditions:

$$\begin{aligned} \alpha_d^2 &= \beta^2 - k_0^2 \varepsilon_d \\ \alpha_m^2 &= \beta^2 - k_0^2 \varepsilon_m \end{aligned} \tag{2.13}$$

The combination of (2.11) and (2.13) gives the dispersion relation for SPPs:

$$\beta = k_0 \sqrt{\frac{\varepsilon_d \varepsilon_m}{\varepsilon_d + \varepsilon_m}} \tag{2.14}$$

To measure the energetic losses of SPPs at a MDI the propagation length is defined as:

$$L_p = \frac{1}{2Im\{\beta\}} \tag{2.15}$$

This is the distance from the point of excitation at which the energy of the surface plasmon is decreased to $\frac{1}{e} \approx 37\%$ of its initial value. The penetration depth of the plasmon into the metal

δ_m and into the dielectric δ_d, in the case of air as dielectric medium ($\varepsilon_d = 1$) are given by [6]:

$$\begin{aligned} \delta_m &= \frac{1}{Re\left\{k_0\sqrt{\frac{-\varepsilon_m^2}{1+\varepsilon_m}}\right\}} \\ \delta_d &= \frac{1}{Re\left\{k_0\sqrt{\frac{-1}{1+\varepsilon_m}}\right\}} \end{aligned} \tag{2.16}$$

High absolute values of the real part of permittivity of the metal thus lead to small penetration depths into the metal and the plasmon instead extends far into the air.

2.2 Surface Plasmon Polariton Excitation

2.2.1 Optical SPP Excitation Schemes

Equations (2.11) and (2.14) implicate that $\beta > k_0\sqrt{\varepsilon_d}$ must be true, which means that SPPs can not be excited directly by light beams at any angle of incidence. To overcome this momentum mismatch special techniques are required. One of the possible approaches is known as prism coupling [15]. A thin metal layer is sandwiched between two dielectric media with different permittivities. Light entering through the higher permittivity dielectric (usually prism-shaped glass) tunnels through the thin metallic layer and excites SPPs at the interface with the lower permittivity dielectric (usually air). Figure 2.3a shows, what is known as the Kretschmann configuration [16], in which the condition for the incident angle of a light beam $k_0\sqrt{\varepsilon_{d1}}\sin\theta$ is:

$$\sin\theta = \frac{1}{\sqrt{\varepsilon_{d1}}}\sqrt{\frac{\varepsilon_{d2}\varepsilon_m}{\varepsilon_{d2}+\varepsilon_m}} \tag{2.17}$$

A possible variation is the Otto configuration [17] in which an air gap is left between the metal layer and the prism in case that direct contact should not be desirable. Another approach for achieving SPP excitation is by grating coupling [15]. The metal surface is patterned with a shallow grating of grooves or holes with lattice constant a. In the one-dimensional case, the

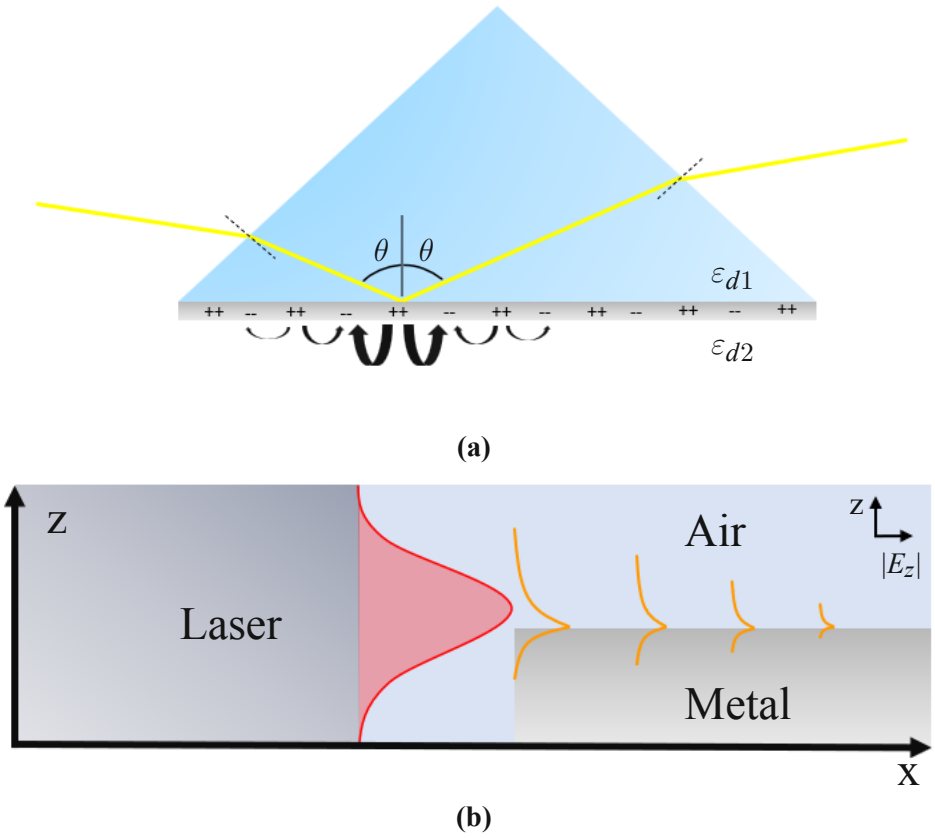

Figure 2.3: (a) Kretschmann configuration for SPP excitation. The bent black arrows illustrate the decaying field of the SPP propagating on the metal-air interface. **(b)** End-fire coupling scheme. The red curve illustrates the absolute of the z-component of the electric field emitted by the laser, while the orange curves indicate the evanescent Field in the z-direction of the excited SPP.

phase-matching condition is given by [15]:

$$\beta = k \sin\theta + m\frac{2\pi}{a} \tag{2.18}$$

with $m = (1, 2, 3, 4...)$ [15]. Coupling efficiencies of gratings reach up to 50% [18]. They can also be used to decouple SPPs from MDIs and it was further demonstrated that focusing of SPPs can be achieved with the proper grating design [19]. Instead of regular grating patterns, also random surface roughness can lead to SPP excitation by providing the neccessary momentum

components δk via scattering under the phase-matching condition:

$$\beta = k \sin\theta + \delta k \tag{2.19}$$

The last optical excitation scheme to be mentioned here is near-field excitation. A small probe tip with an aperture size smaller than the wavelength of the SPP to be excited illuminates the metal surface in the near field. Due to the small aperture size, the light emitted from the tip consists of wave vector components $k > \beta > k_0$, thus allowing phase-matched excitation of SPPs with propagation constant β. [15]

2.2.2 End-Fire coupling

The above-mentioned methods for SPP excitation are limited to small frequency selected through their geometry. The end-fire coupling scheme offers broadband coupling suitable for on-chip devices. With this method SPPs are excited directly by illuminating the MDI with a laser from the side (Figure 2.3b). The coupling efficiency depends on the overlap F between the Field of the incoming beam ($g(\vec{r})$) and the SPP field ($f(\vec{r})$) at the boundary [20]:

$$F = \frac{\int_{-\infty}^{\infty} f(\vec{r}) g(\vec{r})^* d\vec{r}}{\left(\int_{-\infty}^{\infty} |f(\vec{r})|^2 d\vec{r}\right)^{\frac{1}{2}} \left(\int_{-\infty}^{\infty} |g(\vec{r})|^2 d\vec{r}\right)^{\frac{1}{2}}} \tag{2.20}$$

Numerical simulation predicts coupling efficiencies around 80% for a Gaussian incident beam with a width roughly matching the width of the SPP in a loss-less waveguide configuration [21]. In real world applications, coupling efficiencies are lower, but the concept is widely used at various wavelengths, including the mid-infrared [20, 22–24].

2.3 Surface Plasmon Polariton Waveguides

The properties of SPPs can be exploited with suitable materials and geometric designs to guide EMWs in so-called plasmonic waveguides. Compared to photonic waveguides, which operate

on the principle of total reflection, plasmonic waveguides offer the advantages of strong field confinement up to the sub-wavelength scale, high surface sensitivity, and a high level of miniaturization. The downsides are high propagation and coupling losses, limiting their applicability for transmission over long distances. The theory of surface plasmons shows a great variety of architectures with different geometries and materials which influence propagation lengths, field enhancement, and confinement depending also on the wavelength. Configurations range from simple rectangular ridges, V-shaped grooves, and Λ-shaped wedges to cylindrical wires (Figure 2.4).

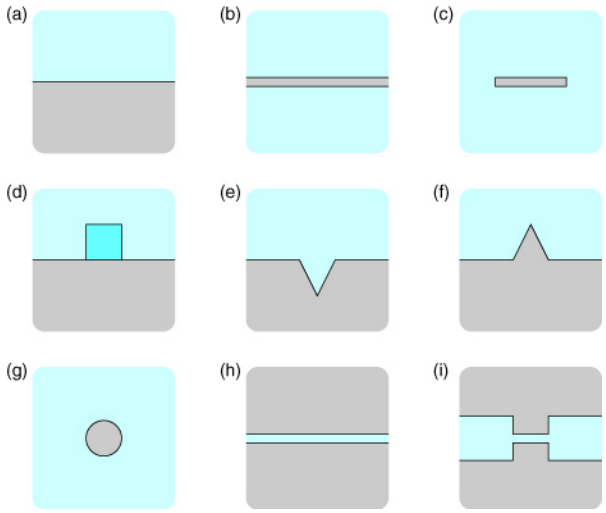

Figure 2.4: Different waveguide configurations, grey and blue areas indicating metal and dielectric media, respectively. Figure taken from [25].

2.3.1 Dielectric Loaded SPP Waveguides

The geometry of an MDI extending infinitely (far with respect to the wavelength) in its plane confines the EMF only in the vertical Dimension. To confine the EMF in two dimensions it is either possible to limit the width of the metal layer (Figure 2.4c) or to limit the width of the dielectric layer intended to guide the SPP modes (Figure 2.4d). The latter configuration is known as a Dielectric-loaded SPP waveguide (DLSPPW). Mode confinement is achieved through the difference in the effective refractive index (n_{eff}) between the loaded and unloaded portions of space above the metal [25]. n_{eff} emerges from considering the different dielectric

media above the metal as one effective optical medium in the direction normal to the metal interface. The propagation constant in this setting can be expressed as $\beta = n_{eff} k_0$. Thus n_{eff} defines the propagation length of the SPP. It can be tuned with the optical properties of the employed materials and the aspect ratio of the dielectric ridge.

The requirements for the WGs in this work are low losses in the mid-IR region and a fairly simple and reproducible processing scheme for on-chip integration. In the mid-IR and LWIR regions, Ge is a relatively easy-to-process dielectric low-loss medium (propagation losses less than 2 *dB*/*cm* between $1.6 - 14.4$ μm [12]), and is therefore chosen for the WG material. Silicon and Polyethylene are other examples of DLSPPW material in the infrared, but come with disadvantages such as lower bandwidth transparency or difficult processing [6, 12]. The WG's

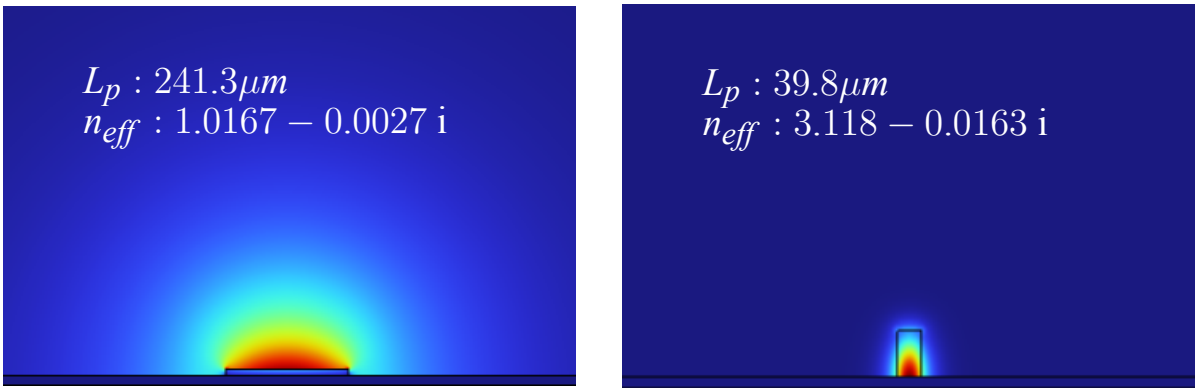

(a) **(b)**

Figure 2.5: SPP-modes in Ge DLSPPWs with **(a)** waveguide dimension of $6\mu m \times 0.3\mu m$ and **(b)** $1\mu m \times 2\mu m$ simulated in COMSOL at a wavelength of $8.2\mu m$. Not the entire simulation domain is shown.

geometry critically influences the mode's behavior. Ge WG simulations show that thin slabs (Figure 2.5a) lead to relatively low losses (16 *dB*/*mm*), with an SPP mode propagating mainly outside the Ge. This weak mode confinement limits the ability of the DLSPPW structure to influence the direction of mode propagation. A thick geometry (Figure 2.5b) instead leads to a well-confined mode within the Ge WG. The mode is guided along the WG even at a small bending radius but suffers from higher losses (110 *dB*/*mm*) due to increased interaction between the mode and the plasmonic materials, such as Au.

3 Mid-Infrared Quantum Cascade Intersubband Devices

In the following chapter quantum cascade lasers (QCLs), quantum cascade detectors (QCDs), and bi-functional quantum cascade laser and detector materials (QCLDs) will be introduced. Its content is mainly based on references [26–30].

3.1 Quantum Cascade Laser

QCLs are semiconductor lasers initially proposed in 1971 by Kazarinov and Suris [31] and firstly demonstrated in 1994 [32]. Today QCL technology covers a broad optical spectrum, which includes multiple atmospheric windows and many fundamental molecular absorption lines, which makes it suitable for sensing applications and free space communication. Today, there are many types of commercially available QCLs ranging from Fabry-Pérot devices, to distributed feedback resonators, and multi-wavelength systems based on tunable external cavities [33–35]. High power continuous wave QCLs at room temperature have been demonstrated with wall-plug efficiencies of up to 21 % [36]. Furthermore, the small dimension of QCLs at the micrometer scale makes them easy to implement for on-chip applications, such as portable bio-sensing devices [37].

3.1.1 Potential Well

The conduction band in QCL and QCD materials is engineered to consist of multiple consecutive potential barriers and wells for electrons. The allowed energy states for a particle inside a potential well with:

$$\begin{aligned} V(x) &= 0 \qquad && x \leq 0,\ x \geq a; \\ V(x) &= \infty \qquad && 0 < x < a \end{aligned} \tag{3.1}$$

are given by the solution of the Schrödinger equation [14]:

$$\left[-\frac{\hbar^2}{2m} \nabla^2(x) + V(x) \right] \Psi(x) = E\Psi(x) \tag{3.2}$$

yielding:

$$\begin{aligned} \Psi(x) &= 0 \qquad && x \leq 0,\ x \geq a; \\ \Psi(x) &= \sqrt{\frac{2}{a}} \sin\left(\frac{n\pi x}{a}\right) \qquad && 0 < x < a \end{aligned} \tag{3.3}$$

for the wave function and:

$$E_n = \frac{\hbar^2 \pi^2}{2ma^2} n^2 \tag{3.4}$$

for the Eigenenergies. $\hbar$ is the reduced Planck constant and m the particle's mass. The probability density of the particle position is given by the absolute square of the wave function (Figure 3.1a). For the particle to be able to transition between two states E_i, E_j the discrete energy difference $\Delta E_{i,j}$ has to be provided, or released depending on whether the final state is at higher or lower energy, respectively. In potential wells with finite potential, the wave function of the particle penetrates the potential domain and decays exponentially. Thus, if two finite potential wells are in close proximity, the particle can either overcome the barrier by gaining enough energy through processes such as photon absorption or scattering, or tunnel through the barrier without changing its current energy level.

3.1.2 Band Structures in Crystalline Solids

Crystalline solids are characterized by regular periodic patterns of their atoms, or ions. Each ion contributes to the potential which defines the energy state of the electrons. The sum of

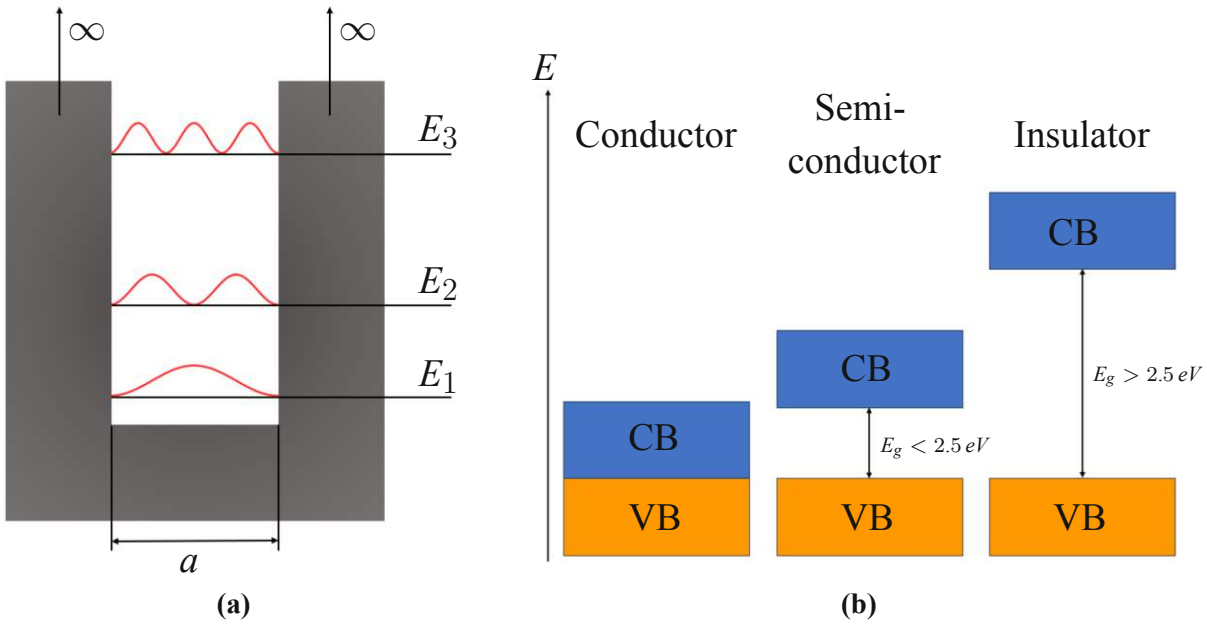

Figure 3.1: (a) Absolute square of the first three wave functions $|\Psi(x)|^2$ of a particle inside a potential well of infinite depth and with width a. **(b)** Schematic energy distribution of valence and conduction band of conductors, semi-conductors and isolators.

these contributions gives the overall potential an electron is subjected to inside the solid if in first approximation the influence of other electrons is neglected. Bloch's theorem states that the potential distribution follows the same periodicity as the lattice, thus:

$$V(\vec{r}) = V(\vec{r} + \vec{R}) \tag{3.5}$$

where $V(\vec{r})$ is the potential at the location $(\vec{r})$ and $\vec{R}$ is the vector of the lattice periodicity. The solution of the Schrödinger equation for a single particle is given by:

$$\Psi(\vec{k}) = e^{i\vec{k}\vec{r}} u(\vec{r}) \tag{3.6}$$

known as Bloch function. It is composed of the function $u(\vec{r})$, which is periodic with the lattice, and a plane wave $e^{i\vec{k}\vec{r}}$. As a consequence of the periodicity of the potential, all necessary information about the dispersion relation of the particle is contained inside one period of the lattice. In momentum space, one such period is called the first Brillouin zone (BZ). Dispersion

relations from all other BZs contribute to the first BZ. This overlap of dispersion relations, together with the condition of periodicity ultimately leads to the formation of the band structure. A band is an almost continuous accumulation of allowed energy states for an electron, with an upper and lower energy limit. Between two bands there may appear a forbidden zone, in which no energy states are accessible for electrons. The highest fully occupied energy band at $0\,K$ is known as the valence band (VB), while the first energy band above the VB at $0\,K$ is called conduction band (CB). In a conductor, the CB is partially filled with electrons which therefore have free states available and thus can move quite freely. In semiconductors the CB is empty at $0\,K$, separated by a gap of usually below $2.5\,eV$ from the VB, while in insulators the gap size is larger than that (Figure 3.1b). Inside a semiconductor an electron can be excited from the VB to the CB, if energy greater or equal to the band gap energy E_g is provided. Due to this interband (IB) transition a positively charged hole is created in the VB. When an electron from the CB recombines with a hole in the VB a photon with wavelength $\lambda_{ph} = \frac{hc}{E_g}$ is typically emitted. This is how conventional laser diodes generate light.

3.1.3 Intersubband transitions

The active region of QCLs consists of periodically alternating layers of different materials, which together form a periodic structure of quantum wells and barriers in the CB. In this structure electrons first tunnel through an injector region which consists of thin quantum wells and then reach the upper energy level of the laser in the gain section (Figure 3.2). In a typical three-level system photons are emitted through optical transitions from the first to the second energy level of the gain section and are then, to ensure population inversion between the first two levels, quickly extracted to the third level through longitudinal optical (LO) phonon-assisted resonant tunneling.[1]. The electrons then proceed to the next period, where the process repeats. Therefore, a single electron emits multiple photons as it crosses the QCL active region, allowing for high power performance and quantum efficiencies greater than one. The transition of an electron between two quantum wells in this subband structure is known as

[1] Figure 3.2 shows the band structure optimized for lasing as well as photodetection and therefore differs from the structure of a typical QCL. Here the extraction from the second energy level occurs through scattering-assisted tunneling.[38]

intersubband (ISB) transition. It can be shown that in the one-band approximation, ISB transitions are subject to selection rules which makes them only sensitive to light polarized in growth direction [39]. Thus QCLs emit TM polarized light. The width of the wells and barriers can be adjusted by varying the heterostructure enabling the tuning of the QCL wavelength. The lower limit is given by the relative CB offsets of the well and barrier material. Thus, QCLs can operate at higher wavelengths as compared to IB lasers, covering the large domain in the infrared mentioned at the beginning of this chapter.

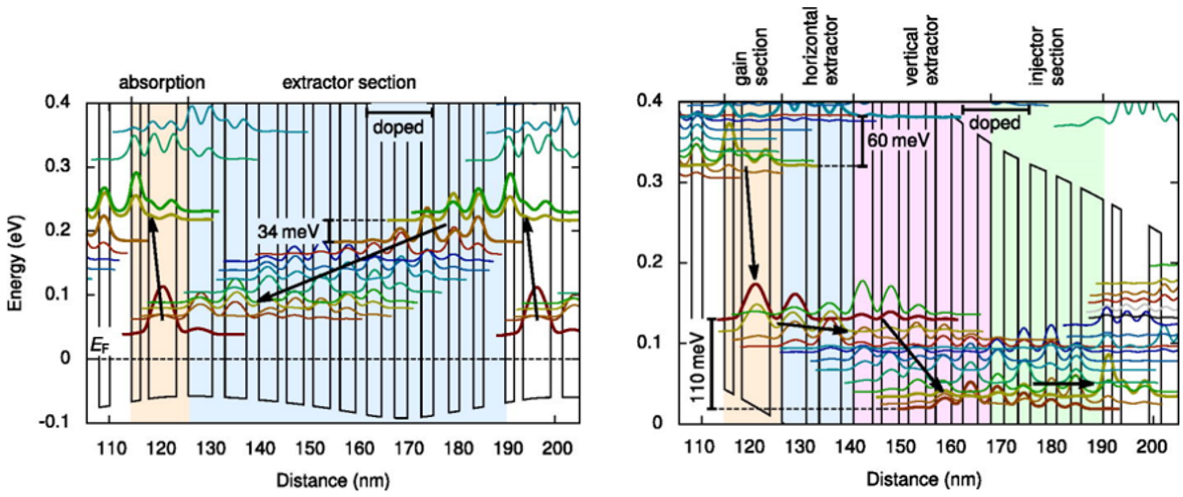

(a) **(b)**

Figure 3.2: Band diagram of a bi-functional QCLD for **(a)** laser bias at the maximum wall-plug efficiency and **(b)** detector (zero) bias. The different logical sections are highlighted in color and the preferred electron transport direction is denoted with black arrows. Figure and description is taken and slightly modified from [38].

3.2 Quantum Cascade Detectors

This section indroduces the QCD and is mainly based on the review paper of Alexandre Delga [40]. The first publication about the operation of a QCL structure as an infrared photodetector was a research article by Hofstetter *et al.* in 2002 [41]. These devices showed poor performance compared to well-developed technologies such as HgCdTe detectors (MCT) and quantum well infrared photodetectors (QWIPs), but the deficiencies were well understood and

following research managed to considerably improve the quantum cascade devices for detection. While MCTs are based on IB transitions, QWIPs and QCDs are both ISB devices. The advantages of ISB detectors are their intrinsic high speed due to the very efficient LO phonon recombination process, with transit time cut-off in the 100 *GHz* range and the fact that they have very high saturation thresholds [42]. On the other hand, they are subjected to the same selection rules for ISB transitions discussed previously. Only photons polarized in growth direction can be detected, which makes it necessary to implement optical coupling structures. QWIPs have simpler band structures than QCLs and are therefore easier to design and process. At their disadvantage they offer fewer tuning options through quantum engineering, or the available choice of material systems and require a bias voltage to operate, leading to dark currents which contribute to dark noise[2] [40]. Since in QCDs, there are usually multiple periods in the band structure of the absorbing region, multiple photons are required to make one electron contribute to the signal current. The amount of electrons contributing to the detector current per incident photon is called the external quantum efficiency (EQE) η. It is linked to the internal quantum efficiency (IQE) η_i by $\eta = \eta_{abs}\eta_i$, where η_{abs} is the ratio between the number of photons absorbed by the detector and the total number of incident photons. The IQE is limited by $\frac{p_e}{N}$, with the probability p_e of an electron to scatter from one period to the next one, after being excited by a photon and the number of periods N in the band structure of the QCD. The number of periods will therefore decrease the IQE, but at the same time increase η_{abs}. Depending on the material and design an optimum N may be found to maximize EQE. The EQE of most QCDs is below $1\,\%$ [40], though there is at least one exception of a single period QCD design of Schwarz *et al.*, which reached $25\,\%$ at room temperature [43]. IB devices instead can reach EQEs close to one, because their absorber region can be designed much thicker[40]. The advantage of QCDs is that multiple periods limit dark noise contributions from thermally excited electrons leading to a better SNR, which is the most important feature of a photodetector.

[2] Signal measured without impinging photons.

3.3 Bi-functional Quantum Cascade Laser and Detector

A bi-functional quantum cascade material at the right geometry and bias functions as QCL, while it works as QCD at 0 bias, with overlapping emission and detection spectra. This opens numerous on-chip applications, such as chemical sensing and heterodyne detection [37, 44–46]. Due to the ISB selection rules both emit and absorb only TM-polarized light and therefore do not require any further coupling schemes. The design challenge for QCLDs is to maintain the spectral overlap between the laser emission and the detector sensitivity. Due to the high bias required for the QCL side, the emission is strongly red-shifted by the Stark effect. In the example of a QCLD subband structure shown in Figure 3.2 wavelength matching is achieved through thicker barriers. At room temperature QCL duty cycles up to 10 % were achieved as well as a detector responsivity of around 40 $\frac{mA}{W}$, which makes those QCLDs comparable to regular high-performance QCLs/QCDs [38].

4 Heterodyne Signal Detection

In the previous chapters, the individual components of the on-chip heterodyne receiver at the center of this work were treated. In this chapter the concept of heterodyne signal detection is introduced and its advantage over direct signal detection at low signal powers is outlined.

In heterodyning two input signals $A_1 \cos(\omega_1 t)$ and $A_2 \cos(\omega_2 t)$ with amplitudes and frequencies A_1, f_1 and A_2, f_2 are combined in a non-linear mixer. In a square-law mixer the resulting signal is [47]:

$$\begin{aligned}(A_1 \cos(\omega_1 t) + A_2 \cos(\omega_2 t))^2 = A_1^2 \cos^2(\omega_1 t) + A_2^2 \cos^2(\omega_2 t) \\ +2A_1 A_2 \cos(\omega_1 t) \cos(\omega_2 t)\end{aligned} \tag{4.1}$$

assuming the same polarization of the EMFs of the signals. The last expression on the right-hand side can be rewritten with the trigonometric identity for the cosine:

$$\cos(a+b) = cos(a)cos(b) - sin(a)sin(b) \tag{4.2}$$

as:

$$A_1 A_2 \left[\cos((\omega_1 - \omega_2)t) + \cos((\omega_1 + \omega_2)t)\right] \tag{4.3}$$

with one high and one low beat note consisting of the sum and the difference of the original frequencies, respectively. At radio frequencies, this has been used for many decades to convert the frequency of an input signal to intermediate frequencies at which useful amplifying devices are available [48]. Forrester in 1961 was the first to suggest employing lasers as local oscillators for optical heterodyning [49]. Applications for optical heterodyning are spectroscopy,

especially in astronomy, wind speed detection through coherent Doppler light detection and ranging measurements, and free space communications [50–52].

The principles of heterodyne detection are explained here following the work of DeLange [53]. In a square-law photodetector, the detector current induced by light with electric field $E = Acos(\omega t)$is given by:

$$i_{dc} = \xi A^2 \cos^2(\omega t) \tag{4.4}$$

The factor ξ is related to the external quantum efficiency by $\xi = \frac{\eta q}{hf}$, with the electron charge q, the Planck constant h and the frequency of the impinging photon f. In the case of a monochromatic signal, the detector current can be expressed through the impinging power P_s as $i = \frac{\eta q P_s}{hf}$. The signal power at the detector is given by its current and resistance:

$$W_D = i^2 R = \xi^2 P_s^2 R \tag{4.5}$$

The current is composed of discrete charges, the photon-activated moving electrons, and therefore it is subjected to shot-noise. If the impinging photons arrive at a mean rate r at the detector, the probability of exactly n photons arriving after the time t follows the Poisson distribution:

$$p_n(t) = \frac{(rt)^n}{n!} \exp^{-rt} \tag{4.6}$$

The root mean square (RMS) dispersion of this distribution is given by:

$$(\delta n)^2 = \tilde{n} \tag{4.7}$$

where $\tilde{n} = rt$ is the expectation value of the number of particles arrived at the time t. The photon photocurrent and its mean value are given then by:

$$\begin{aligned} i &= \frac{nq}{T}; \\ \tilde{i} &= \frac{\tilde{n}q}{T} \end{aligned} \tag{4.8}$$

with the observation time T. The RMS deviation is then:

$$(\delta i)^2 = \frac{q^2}{T^2}(\delta n)^2 = \frac{q^2}{T^2}\tilde{n} = \frac{q}{T}I \tag{4.9}$$

By choosing to observe the current after a low-pass filter with spectral response:

$$F(\nu) = \frac{\sin \pi\nu T}{\pi\nu} \exp^{-i\pi\nu T} \tag{4.10}$$

the bandwidth is obtained with:

$$b = \int_0^\infty |F(\nu)|^2 d\nu = \frac{1}{2T} \tag{4.11}$$

Substituting T with $\frac{1}{2b}$ in equation 4.9 finally leads to the expression for shot-noise current at bandwidth b:

$$(i_{sn})^2 = 2qbi_{dc} = \frac{2\eta q^2 b P_s}{hf} \tag{4.12}$$

For a more detailed derivation of shot-noise see [54]. The SNR is therefore:

$$\frac{S}{N} = \frac{i^2}{(i_{sn})^2} = \frac{\eta P_s}{2hfb} \tag{4.13}$$

and represents the highest achievable SNR in an ideal direct detector in an otherwise noise-free environment. In real devices and environments, other noise such as thermal noise and dark-current noise are present. These do not depend on P_s and therefore can therefore be greater than the input signal. This often is the case in free-space communication where the source of the signal is at a great distance from the detector. In such a setting heterodyne signal detection becomes advantageous. When a weak input signal with $E_s = A_s \cos(\omega_s t)$ together with background signals $E_B = \sum A_k \cos(\omega_k t)$ is combined with a strong signal of a local oscillator $E_o = A_o \cos(\omega_o t)$, the resulting field is the sum of all components and the detector current therefore:

$$i = \xi \left(A_s \cos(\omega_s t) + A_o \cos(\omega_o t) + \sum A_k \cos(\omega_k t) \right)^2 \tag{4.14}$$

In good approximation one may neglect the usually small contributions of cross products and beatings involving $\sum A_k \cos(\omega_k t)$ together with the sum of frequency terms, which are too high for detection. The detector current can then be expressed through:

$$i = \xi \left(\frac{1}{2}(A_s^2 + A_o^2 + \sum A_k^2) + A_s A_o \cos((\omega_o - \omega_s)t) \right) \tag{4.15}$$

The detector signal thus consists of a direct current portion proportional to the sum of the powers of the local oscillator, the input signal, and the total background, and an oscillating current representing the beating between the local oscillator and the input signal. From equation 4.12 one can write the shot-noise current for this case:

$$(i_{sn})^2 = \frac{2\eta q^2 b}{hf}(P_s + P_o + P_B) \tag{4.16}$$

For $P_o >> P_s$ the shot-noise is considerably higher in a heterodyne receiver (equation 4.16) compared to a direct detector (equation 4.12), but also the signal power is amplified. The intermediate frequency (IF) current is obtained from equation 4.15 and given as:

$$i_{IF} = \xi A_s A_o \cos((\omega_o - \omega_s)t) \tag{4.17}$$

The resulting IF power is:

$$P_{IF} = (i_{IF})^2 R = 2\xi^2 P_o P_s R \tag{4.18}$$

and the carrier-to-noise ratio:

$$\frac{C}{N} = \frac{(i_{IF})^2}{(i_N)^2} = \frac{\xi P_o P_s}{qb(P_s + P_o + P_B) + N_T} \tag{4.19}$$

Here a thermal noise component N_T is introduced, which depends only on temperature but not on the input signal power. For transmissions over far distances, the input signal can be orders of magnitude below N_T, and therefore can not be easily detected directly. The power of the LO can usually be made much higher than N_T and $P_s + P_B$, therefore $qbP_o >> qb(P_s + P_B) + N_T$.

Thus the expression above is well-approximated by:

$$\frac{C}{N} = \frac{\xi P_s}{qb} = \frac{\eta P_s}{hfb} \tag{4.20}$$

Thus while the shot-noise current increases with P_o, the SNR remains proportional only to P_s. The comparison between equations 4.5 and 4.18 shows that the signal in the heterodyne setup is amplified by a factor of $K\frac{P_o}{P_s}$, where K is a constant. For weak input signals and strong local oscillators, this gain can be of many orders of magnitude. Further, the contributions of background signal and thermal noise, which in a direct detector would exceed the power of the input signal, in the heterodyne configuration can become negligibly small, and the SNR may approach the optimum possible value. The advantages of heterodyne signal detection are convincing, but there are criteria to be met to obtain it. For the input signal to properly overlap with the local oscillator, they must have the same mode structure, which in general limits the operation to the fundamental mode. Further, the beams of the two signals need to overlap at the detector and propagate in the same direction. At last, the wavefronts must be of the same curvature and the same polarization. It appears not to be an easy task to guarantee all these criteria to be met, yet in the on-chip QCLD design with DLSPPWs for beam combination employed in this work, they are intrinsically fulfilled. Only the direction of beam propagation is slightly different, but due to the small detector surface and the Au covering, the signals still overlap through the detector.

5 Waveguide Simulations

The aim to model a monolithically grown on-chip heterodyne receiver requires a waveguide structure which combines the external signal coupled and amplified through a QCL functioning as SOA with the signal of the LO and then couples the combined signal to the QCD. In this work the two waveguide geometries shown in Figure 2.5 have been investigated and compared. Before processing the actual devices, the Wave Optics Module of the *COMSOL Multiphysics* Simulation Software has been employed to predict optical losses.

5.1 Wave Optics Simulations in COMSOL

In COMSOL the partial differential equation [55]:

$$\left(\nabla - i\vec{k}\right) \times \mu_r^{-1} \left(\left(\nabla - i\vec{k}\right) \times \vec{E}\right) - k_0^2 \left(\varepsilon_r - \frac{i\sigma}{\omega\varepsilon_0}\right) \vec{E} = 0 \tag{5.1}$$

is numerically solved by applying the finite element method (FEM). k_0 denotes the wavenumber of the incident EMW in vacuum and σ the electrical conductivity. The FEM approximates the dependent variables of the partial differential equation, in this case, the electrical field vector $\vec{E}$, with functions consisting of a linear combination of functions and coefficients limited to certain points in space and their close surrounding, which is defined by a mesh. The continuous physical entities thus are discretized and the accuracy of the result depends on the strength of the variation of the variables in space combined with the grid density of the mesh. At the borders of the physical domain, suitable boundary conditions have to be introduced. To avoid non-physical reflections of optical fields reaching significantly beyond the simulation domain perfectly matched layers can be introduced at the boundaries. They represent an additional

layer that acts as a perfect absorber, mimicking an infinite extension of the domain. A detailed description of the FEM is found on the *COMSOL* website [56].

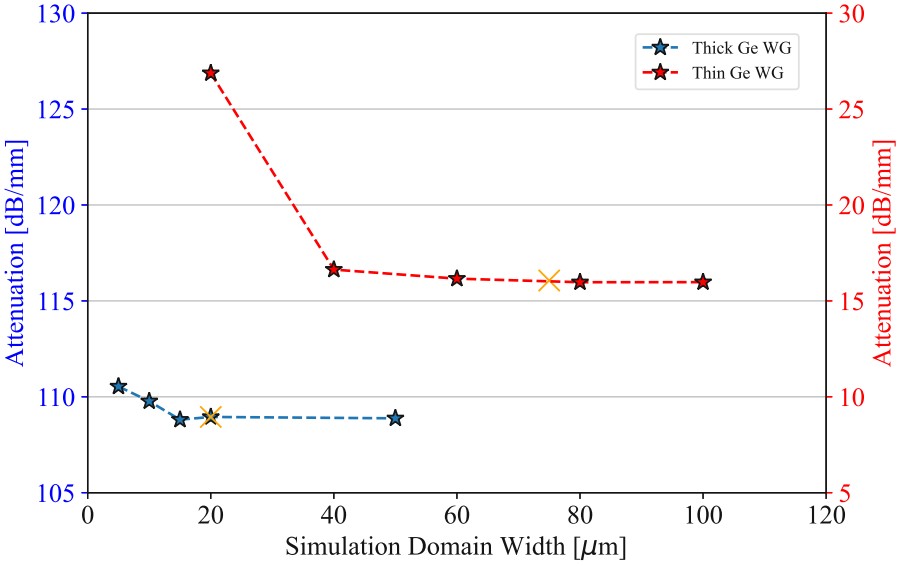

Figure 5.1: Convergency tests from 3D-simulations to establish a suitable simulation domain size. The orange x marks the value of the domain width used for all further simulations. To reduce the domain size perfectly matched layers were introduced in the thin Ge simulations.

The input parameters for the simulations consist of the geometry, the mesh density and shape, the wavelength of interest and the relative permittivities of the materials. The latter were obtained through ellipsometry measurements by Stefania Ischeri at the Central European Institute of Technology in Brno (Appendix 9.1). To ensure a large enough simulation domain size, convergency tests were performed (Figure 5.1), in which the domain is continuously increased until the solutions reach stable values. As already discussed in section 2.3.1 the thin Ge WG geometry results in only weakly bound SPPs, which therefore extend far from the WG requiring a larger simulation domain. Attenuation $\alpha[dB/mm]$ is the figure of merit chosen in this work to evaluate the WG performance. It is obtained in the simulations through:

$$\alpha = -\frac{S_{12}}{l_{WG}} = -\frac{20\log\left(\frac{I}{I_0}\right)}{l_{WG}} \tag{5.2}$$

where the S-parameter is a direct output of the simulation evaluating the total loss of energy between input and output port[1] in dB and l_{WG} is the length of the WG. The equivalent expression at the right shows how the S-parameter is connected with the initial field intensity I_0 and the intensity at the end of the WG I.

5.2 Thick Germanium Waveguides

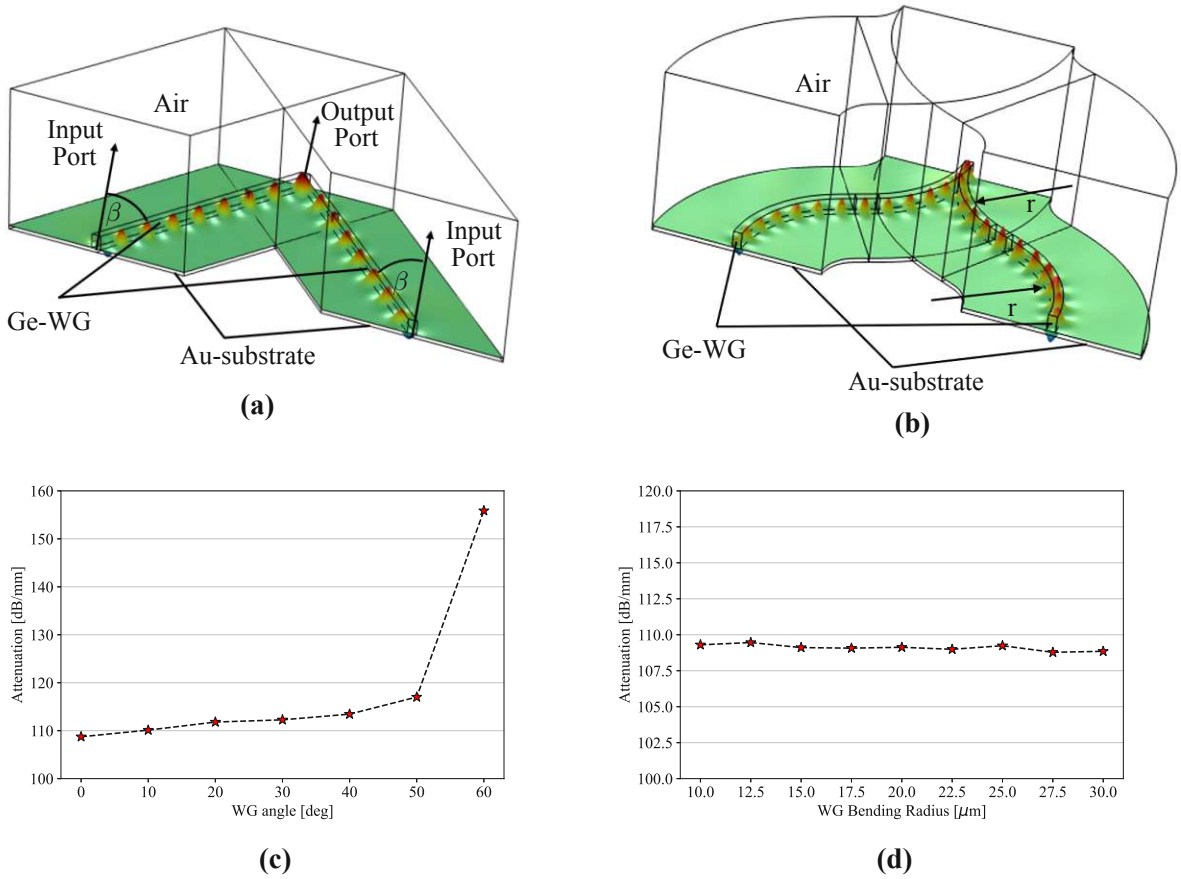

Figure 5.2: (a) V-shaped beam combiner with angle β between WG and incident beam. The black arrows show vectors normal to the input and output port faces of the simulation domain. **(b)** S-bend beam combiner with bending radius r. The black frames indicate the simulation domain and the colors represent the value of the z-component of the electrical field on the gold surface.[2] **(c)** Attenuation of a linear WG at different angles β. **(d)** Attenuation of a $90°$ circular WG at different radii r.

[1] In Comsol ports are boundary conditions at which electromagnetic energy enters or exits the simulation domain.

In the thick Ge WG configuration (1x2 μm) the SPP mode is well confined inside the WG due to the high effective index around 3.1. This leads to high interaction between the SPP and the plasmonic Au substrate leading to very high losses of 108.7 dB/mm in a linear WG ridge at a wavelength of 8.2 μm. For the heterodyne beam combination two designs illustrated in Figure (5.2a,5.2b) were investigated. In the V-shaped design the shortest path between QCLs and QCD is taken, minimizing the WG length. Simulation suggests though that larger angles β between the WG and the incident beam lead to higher attenuation, especially above $50°$. The losses per length of the circularly bent WG design on the other hand is nearly independent of the bending radius. According to these results, the more favorable design depends on the relative positions of QCL and QCD facets. Regarding the response to different wavelengths simulations show very stable behavior in the range between $8 - 8.5$ μm (Figure 5.3). Thus broadband applications are not expected to be affected in this region by the spectral response of the WG.

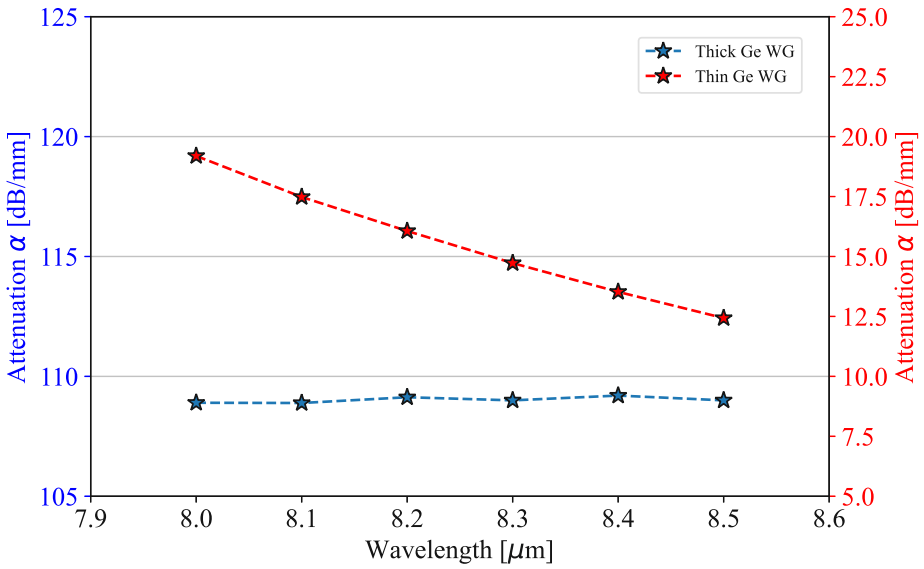

Figure 5.3: 2D Simulation results at different wavelengths for the thick and the thin WG design.

[2] In COMSOL it is not possible to excite 2 ports simultaneously. Therefore, these two figures serve only illustrative purposes and result from simulations with one excited port at the top.

5.3 Thin Germanium Waveguides with integrated Gold Mirrors

The thin Ge-WG geometry offers low losses around 16 *dB*/*mm* as well as a larger interface between Gold and Ge-WG for coupling the QCL field to the WG. With an $|n_{eff}| \approx 1.014$ close to one the SPP is just weakly bound to the WG and is not able to follow bends in its structure (Figure 5.4a). Therefore, a Gold coated structure is introduced as a mirror to redirect the SPPs propagation (see Figure 5.4b). For this approach simulations of one mirror redirecting the SPP by $90°$ at different mirror parameters were performed to gather information for the processing. The graph in Figure 5.4c shows the results of these simulations, where the losses attributed to the mirror were obtained by subtracting the losses of the linear WG from the total losses. While one parameter is varied the others are kept at the parameters: $gapsize = 0.5\ \mu m$, $mirrorheight = 6.5\ \mu m$, and $mirrorwidth = 28.5\ \mu m$. The gap size denominates the shortest distance between the mirror surface and the WG and does not strongly influence the losses up to $2\ \mu m$, which can easily be realized in the processing of the devices. The height of the mirror significantly affects losses for values below $8\ \mu m$. As will be discussed in more detail in section 6.1, due to the monolithic process the height of the mirror is limited to the thickness of the QCLD material between the active region and the top cladding. The maximum mirror height to be achieved, thus results in $6.5\ \mu m$, which is still acceptable regarding losses. For the width of the mirror, simulations show that losses are low above $25\ \mu m$. Analyzing these results, the expected losses due to one Gold mirror with realizable parameters are 2.2 *dB*. Comparing the thin Ge WG geometry (16 *dB*/*mm*) with two integrated Gold mirrors (4.4 *dB*) to the thick Ge WG design (109 *dB*/*mm*) the first becomes more favorable at WG lengths above $47\ \mu m$. Coupling losses and additional losses due to imperfections in the structures are not included in this comparison and can have a considerable impact on these results. Regarding the spectral behavior of the thin Ge WG within the range shown in Figure 5.3, α varies by almost 7 *dB*/*mm*. Depending on the WG length and the device's bandwidth this might be a factor to be taken into consideration.

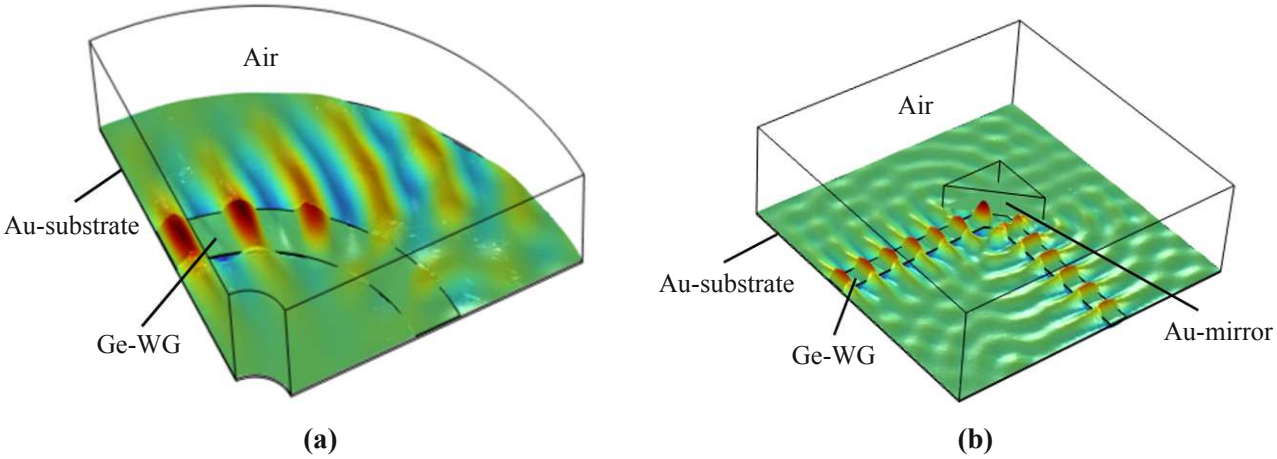

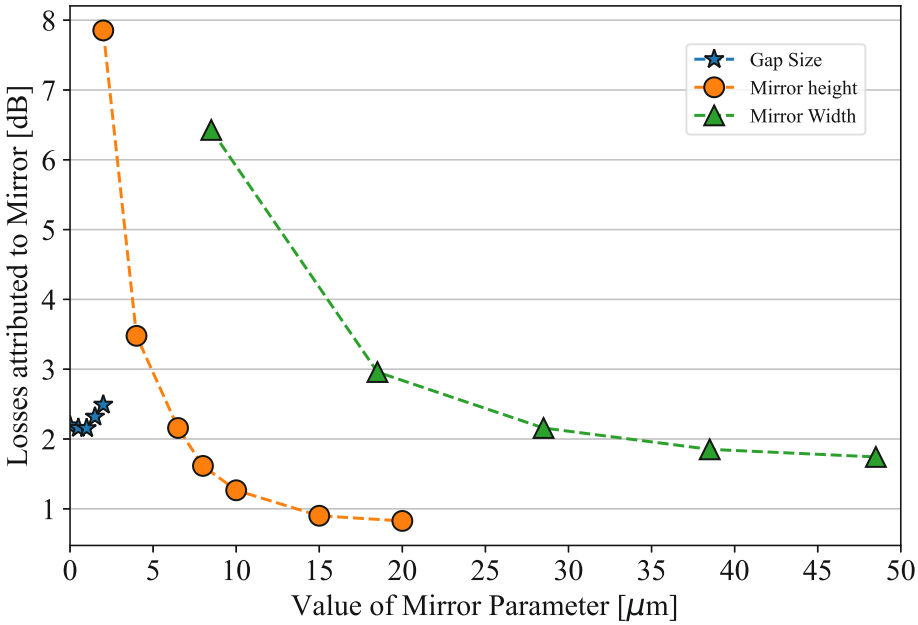

(c)

Figure 5.4: (a) SPP propagating along a $90°$ circular thin Ge-WG ($6x0.3\ \mu m$). The SPP mode is not able to follow the WG due to the low n_{eff} of 1.014. **b** SPP mode getting redirected by $90°$ at a Au micro-mirror structure. The illustrated simulations are performed at a wavelength of $8.2\ \mu m$. The black frames indicate the simulation domain and the colors represent the value of the z-component of the electrical field on the gold surface.**(c)** Losses attributed to a Gold mirror at different parameters.

6 Device Fabrication

The QCLD Material was designed at the *Institute of Solid State Electronics* (*FKE*) at *TU Wien* and grown by MBE and MCOVD at *III-V Lab* in Paris. Its active region is based on GaInAs and AlInAs, whereas the cladding and the substrate consist of doped InP. The fabrication of the devices was performed at the *ZMNS*, a state-of-the-art cleanroom available to the *FKE* at *TU Wien*. The first generation of devices performed poorly, with many QCLs, or QCDs not operating. Furthermore, Au covering the mirror structures and plasmonic Au below the Ge WGs detached in many devices, disabling mirror operation and interrupting WGs (Appendix 9.2). In the second generation improvements in the fabrication, such as the process of the mirror coating, QCL thickness, and the introduction of separated bottom contacts for QCLs and QCDs were successfully implemented. This chapter describes the steps and techniques of the improved processing and presents the resulting devices.

6.1 Fabrication Process

First $1\ \mu m$ of SiN is deposited on the QCLD sample through plasma-enhanced chemical vapor deposition. A hardmask with the features of QCL, QCD, and mirror structures is then predefined through photolithography (PL) and finalized with a CHF_3 reactive-ion etch (RIE). After removal of the residual resist with Acetone and Isopropanol $8\ \mu m$ of the QCLD material are removed by Cl_2-Ar deep etching. To electrically isolate the surface a $250\ nm$ thick SiN passivation layer is deposited. Through PL and RIE process the SiN passivation is opened at the top of the QCLD ridges for the top contacts. Another PL is performed before $10\ nm$ of Ti and $300\ nm$ of Au are sputtered on the sample. In a lift-off undesired Au is removed, finalizing the

top contacts on the ridges. To free QCL and QCD facets covered by the SiN passivation a RIE SF_6 etch is performed. To cover the mirror structures 10 *nm* Ti and 30 *nm* Au are sputtered on the sample after PL. Undesired Au is removed with a lift-off. Then bottom contacts and the Ge WG's plasmonically active substrate are defined through PL and 10 *nm* of Ti and 350 *nm* of Au are evaporated on the sample. A lift-off finalizes the step. Finally, the WGs are defined through PL, Ge of a thickness according to the design (2 μm, or 300 *nm*) is sputtered on the Sample and etched with SF_6. In the last step, the back facets of the QCLs, which are not foreseen as local oscillators are cleaved open. Figures 6.1 and 6.2 show various configurations of the 2nd generation. The thin Ge devices in Figure 6.1 are well fabricated. The etching of the thick Ge WGs at such a high aspect ratio (1×2 μm) instead proves difficult. Since WG losses in the thick Ge are intrinsically high and the mode is confined almost entirely to the small cross-section of the WG, a high quality of the structure is important. The grooves, bulges, and accumulations of Ge close to the facets seen in the SEM pictures, therefore, explain why the general performance of these devices was poor.

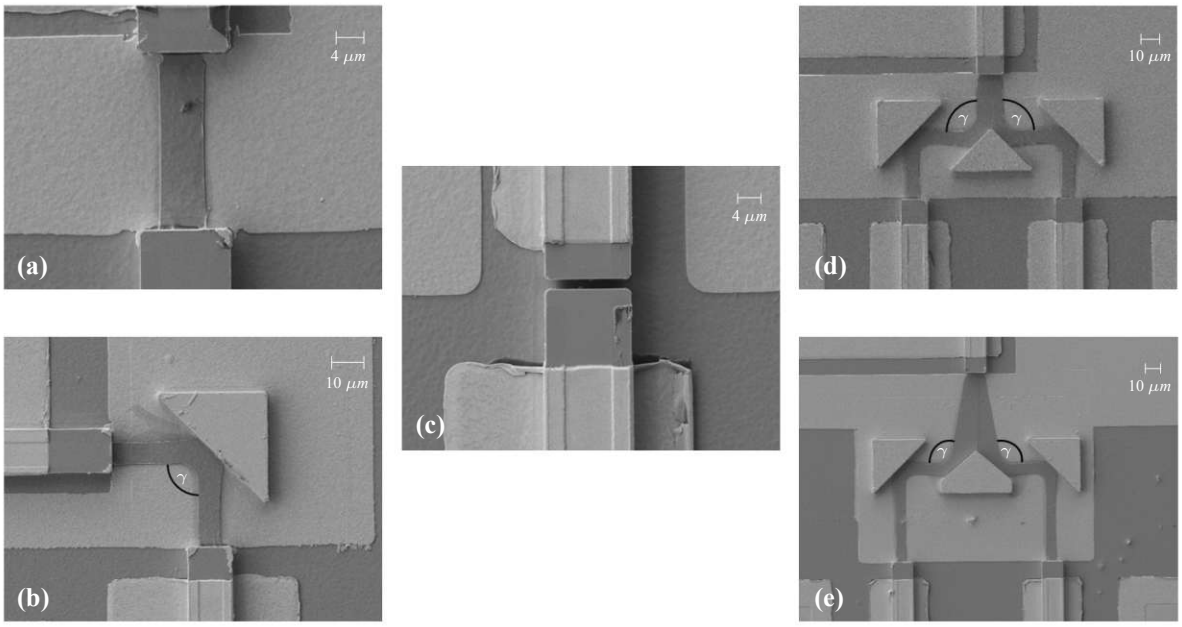

Figure 6.1: SEM images of fabricated 2nd Generation thin Ge-WG designs. **(a)** Linear Ge-WG design (Lin). **(b)** $\gamma = 90°$ single mirror design ($90°$ SM). **(c)** Linear design without WG and 2 μm wide gap for reference. **(d)**,**(e)** Heterodyne detector design with $\gamma = 90°$ ($90°$ HD) and $\gamma = 100°$ ($100°$ HD).

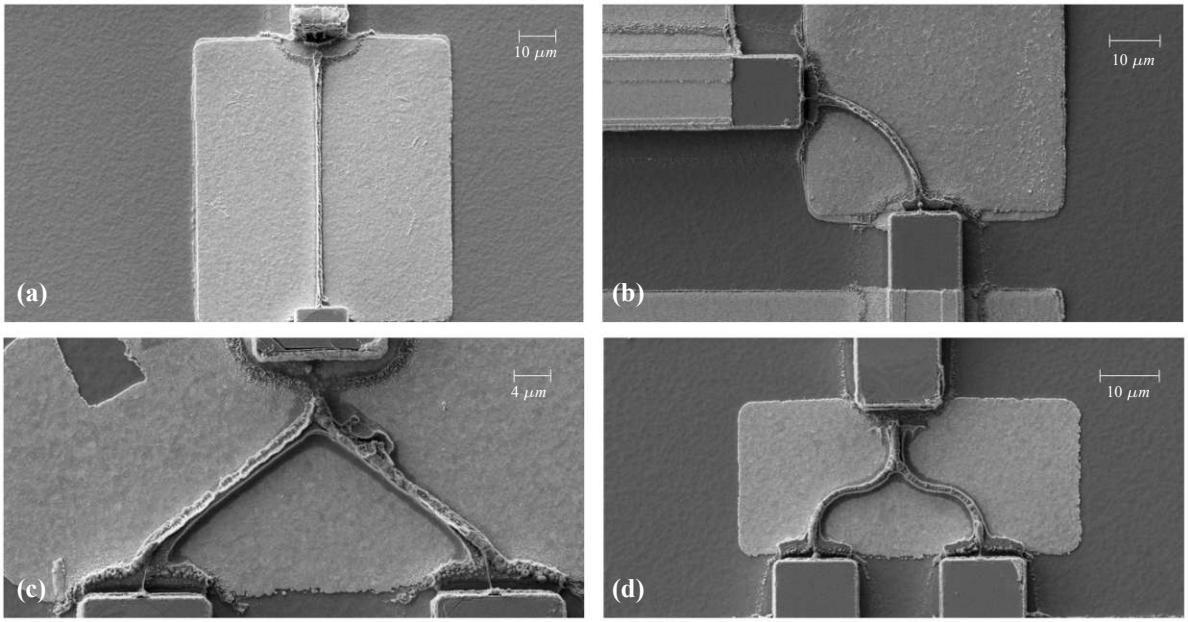

Figure 6.2: SEM images of fabricated 2nd Generation thick Ge-WG designs. **(a)** Linear Ge-WG design (Lin). **(b)** 90°-bend design. **(c)** Linear heterodyne design. **(d)** S-bend heterodyne design.

7 On-Chip Waveguide Characterization

7.1 Methods

In the simulations, perfect materials without defects, or other imperfections are assumed and only the optical losses originating from the electrical properties of the materials are studied. In the physical devices, there are three sources for optical losses connected to the WGs: coupling losses between QCL and WG and WG and QCD, WG losses due to dampening of the EM field in the WG material as studied in the simulations, and scattering losses due to imperfections in the WGs geometry. To characterize these losses an approach resembling the effective cutback technique applied by David *et al.* in a previous work on Ge DLSPPWGs [24] is chosen. In the classical cutback technique, a WG is continuously shortened by cutting it off. At each length, the transmitted signal of an external light source is measured. WG and coupling losses are obtained from a linear fit to the data as slope and offset respectively. In this work multiple linear WGs, as shown in Figure 6.1a are fabricated at different lengths by applying the same fabrication process. It is shown in [24] that the assumption of identical optical properties among such WGs can yield results that are in good agreement with simulations. As a reference, some devices are fabricated without WG and small gaps of 1-4 μm between QCL and QCD (Figure 6.1c). The strongest signal measured in these devices is chosen and considered to be reduced only insignificantly by coupling losses and attenuation. In this work, however, the WGs are integrated between a QCL and a QCD. Thus, the light source and the detector differ for each WG. The advantages of this approach are that no alignment between laser, WG, and detector is required and the possibility to estimate QCL-WG-QCD coupling losses, which are intrinsic to the devices. The cost is higher uncertainty due to imperfections affecting also QCLs

and QCDs, electrical cross-talk between QCL and QCD, as well as other issues which will be discussed in detail in section 7.2.

7.1.1 Experimental Setup

A sketch of the experimental setup for the WG characterization is shown in Figure 7.1. For the light-current-voltage measurement (LIV) a HgCdTe Vigo System PVMI-4TE-8 photodetector (MCT) is aligned to the open QCL back-facet. Since these QCLs do not work in continuous wave operation at room temperature due to thermal limitations of the devices, they are driven in pulsed mode at a frequency of 1 *kHz* and a pulse width of 1 μs with an HP 8114A pulse generator. QCL current, QCD signal, and MCT signal are measured with a Tektronix TDS 2024C Oscilloscope. The electrical contact between on-chip devices, pulser, and oscilloscope is established via needles put onto the top (TC) and bottom contacts (BC) of the QCL and QCD. The sample stage consists of a Cu sample holder with an integrated Peltier cooler to keep a temperature of 17°*C*. It is mounted on an x-y-z stage for alignment between QCL facet and MCT.

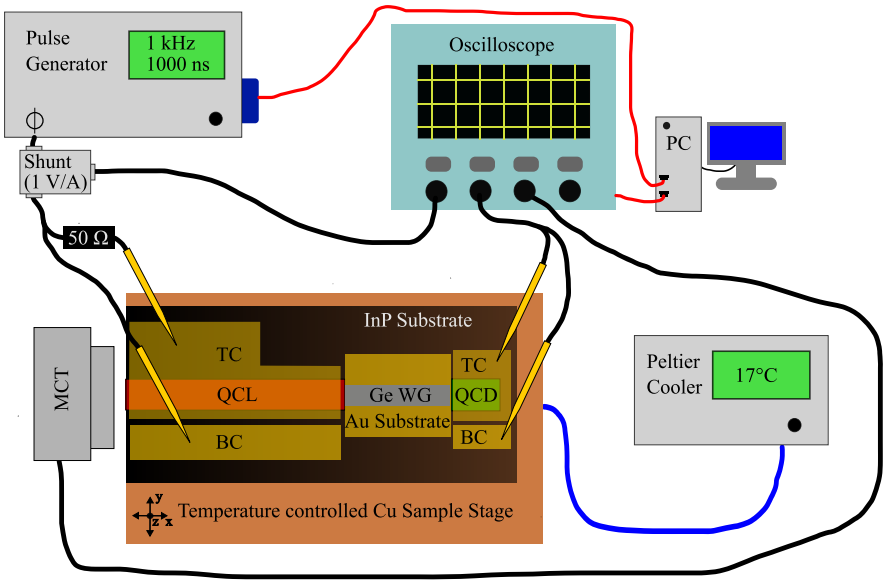

Figure 7.1: Experimental setup for PDMs.

7.1.2 Photodetector Measurements (PDM)

For the PDMs the voltage supplied by the pulser, starting from $-2\ V$, is decreased in steps of $2\ V$ beyond the point of the maximum output power of the QCL.[1] Figure 7.2 illustrates data of one PDM. The values are the averaged root mean squares of the signals over one pulsewidth, obtained with the oscilloscope. The blue stars indicate the signal measured with the on-chip QCD. Initially, it increases almost linearly with the QCL current, due to crosstalk. As the QCL starts lasing, the MCT signal (red +) starts to increase and the slope of the QCD signal changes significantly. At higher currents the slopes of the MCT and QCD signal decrease, as the QCL reaches its maximum output power. This is due to negative differential resistance. In the QCL, negative differential resistance is a direct consequence of misalignments in its discrete energy-level structure and leads to decreasing current at increasing voltage [29]. A reduction of current conducted through the QCL leads to decreased laser power and therefore, lower detector signal. Around the current at which lasing starts the signals of the MCT and the QCD are well approximated by linear functions. The calibrated QCD signal associated with the detection of the laser emission in this domain is obtained through the subtraction of the pink dashed line from the orange one. The QCL current at an MCT signal of 0.3 is chosen to evaluate the calibrated QCD signal for each device.

7.2 Results

The losses of the WGs are calculated as follows:

$$\alpha_{tot} = 20 * \log\left(\frac{U_{WG}}{U_{REF}}\right) \tag{7.1}$$

Here U_{WG} and U_{REF} are the values of the QCD signal from the device with WG and the reference device without WG obtained from PDMs as described above. The results are for the thing Ge WG design is shown in Figure 7.3. The blue diamonds indicate the mean values of the linear WG devices at the respective WG lengths. The black dotted line represents a lin-

[1] Electrons are the charge carriers in QCLs, thus a negative voltage has to be applied between the top and the bottom contact.

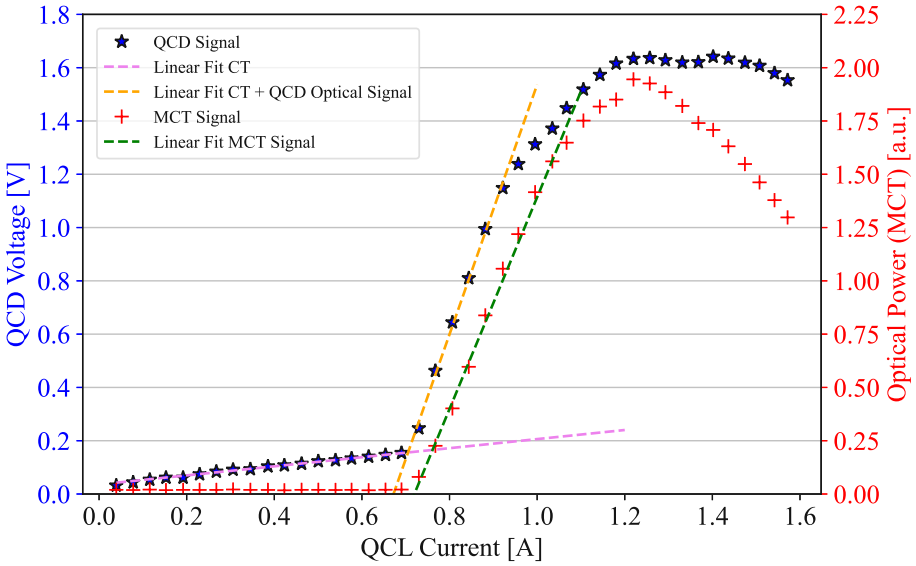

Figure 7.2: Internal and external photodetector signals of a linear thin Ge WG configuration.

ear fit to this data. The slope corresponds to the WG losses and has a value of 18.35 *dB*/*mm*, while the coupling losses correspond to the offset of the line at 7.21 *dB*/*mm*. The purple area which widens toward higher WG lengths represents the simulation results for thin Ge at wavelengths between 8 and 8.3 μm. Even though there is considerable uncertainty in the data, the value extracted from measurements fits the simulation surprisingly well. Differently colored data points indicate designs with integrated gold mirrors. To obtain an estimation of losses attributed to the different mirror designs, the above-obtained coupling and WG losses are subtracted from the measured α_{tot}. For each design, the mean value is taken and defined as mirror losses α_M. In the graph $\alpha_{tot} - \alpha_M$ is shown, with the standard deviation of α_{tot} at the corresponding WG length. Compared to the simulations, mirror losses in the real devices are 5 *dB* higher for the single mirror. Since the use of gold mirrors to redirect SPPs in the mid-infrared is a new concept there are no concrete hints in literature to explain this significant discrepancy. Possibilities are reflections from domain boundaries in the simulation and high absorption or scattering losses from the sputtered gold on the mirrors. Further work is required to investigate this issue in detail. The data though sustains qualitatively two expectations. First, the 100° heterodyne device with two mirrors shows about twice the losses of the single mirror

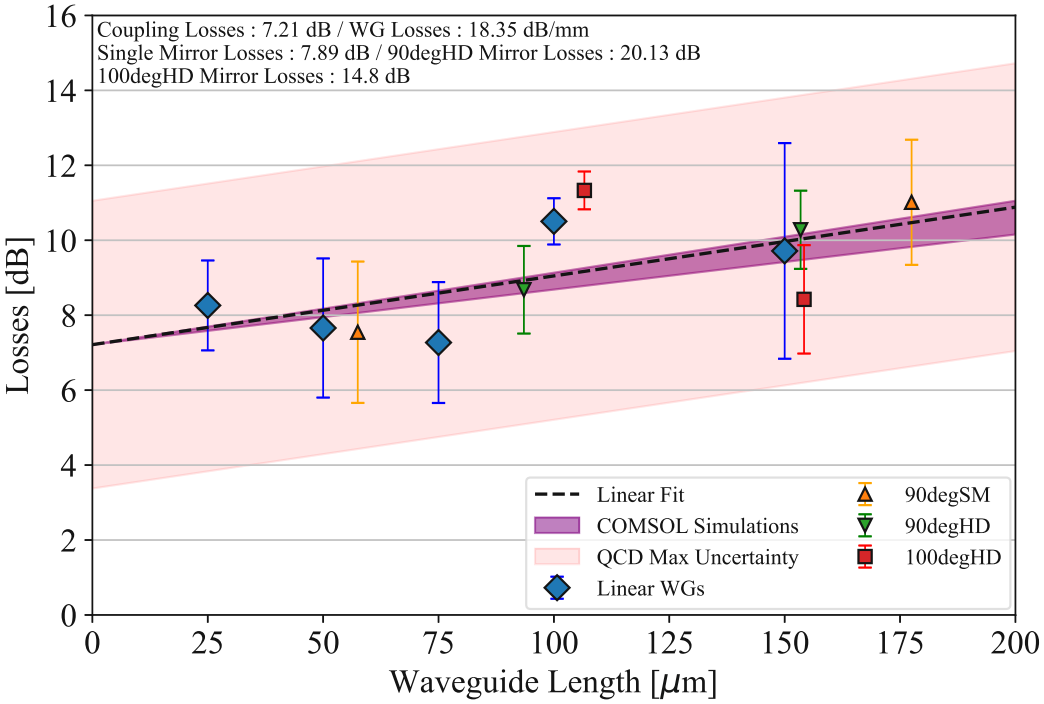

Figure 7.3: Experimental results for the losses of thin Ge devices. Each point of measurement represents the mean value of at least three devices, while the error bars show the corresponding standard deviation.

device. Second the 100° (Figure 6.1e) heterodyne design's performance exceeds the 90° (Figure 6.1d) . In the first the SPP meets the second mirror at its center, thus most of the wide modes energy can be redirected toward the QCD. In the 90° design the WG is on the edge of the second mirror, thus part of the mode's center which contains most of its energy is lost, as it continues to propagate straight on. The indicated deviations in Figure 7.3 reach up to 3 *dB* even for the linear devices without a mirror. Possible explanations are great variations in the WG quality, different QCL wavelengths, and different QCD responsivities. The first reason is unlikely since all WGs were processed in the same way and SEM images do not show grave differences in their quality.

7.2.1 QCL spectra

Regarding QCL wavelengths the simulation results seen in Figure 5.3 for the thin Ge show that a difference of 500 *nm* in wavelength corresponds to a 7 *dB*/*mm* difference in WG losses. Thus at a maximum WG length of 150 μm losses may differ by 1 *dB* in the worst case within the given wavelength range. FTIR measurements of the QCLs show that the QCL's emission varies between 8 and 8.3 μm, which may affect losses within the purple area and thus can not explain the high uncertainty of the data. It can be seen in Figure 7.4 that mode hopping occurs in the QCLs, causing a shift in the wavelength at increasing currents. This well-known phenomenon in semiconductor lasers is often caused by rising temperature affecting the behavior of the gain medium stronger than the cavity resonances [57]. Still, the observed variations caused by mode hopping are well below 500 *nm* and therefore not sufficient to explain the high uncertainty of the data.

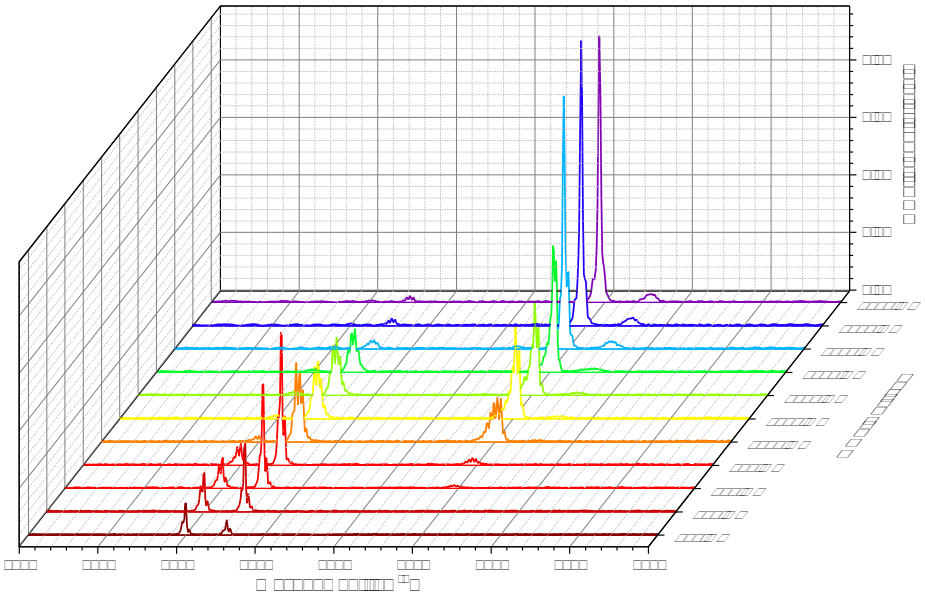

Figure 7.4: FTIR spectra of a QCL at different current.

7.2.2 QCD spectral response

To characterize the QCD's spectral response two free-standing QCDs are fabricated at the edge of the sample with an open facet towards the outside. The beam of a pulsed External Cavity QCL (EC-QCL) (Daylight Solutions 11088) tunable from 8.06 to 11.24 μm is focused via a parabolic mirror and aligned to the QCDs' facet. A wavelength sweep of the EC-QCL is performed at 4 *kHz* frequency and 500 *ns* pulse width. The signal is detected by a Lock-In amplifier (*EG&G Instruments 7265 DSP LOCK-IN*) and recorded. Figure 7.5 shows the result of this wavelength sweep. The presented data is calibrated to the EC-QCL's power spectrum (Appendix 9.3) and normalized to the maximum value. There is a clear interference pattern

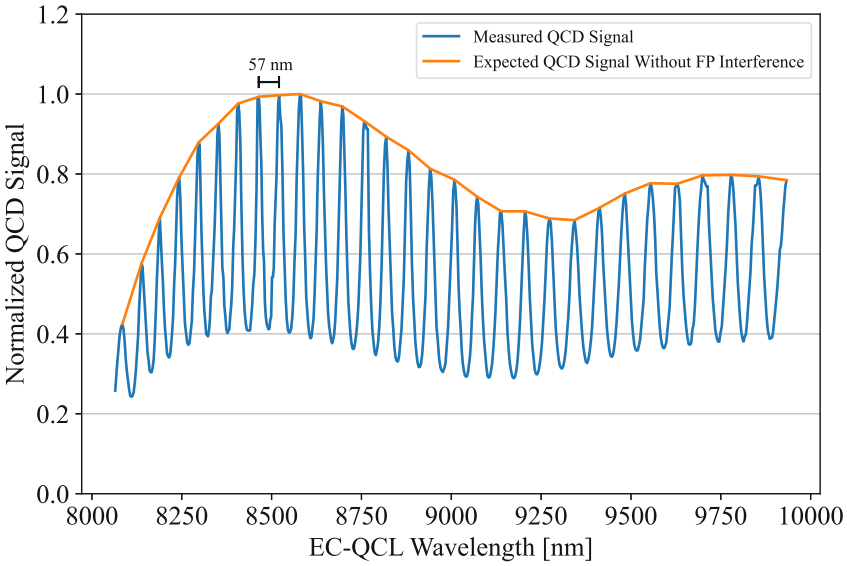

Figure 7.5: Spectral response of a calibrated and normalized 200 μm long QCD.

with 57 *nm* wide fringes. Within the wavelength range of $8 - 8.3$ μm the signal at the minima is up to 60 % lower than at the adjacent maxima. The orange line represents the upper limit of the interference pattern and corresponds to the expected QCD response without interference. A reduction to 40 % translates to 7.8 *dB* lower energy. This is illustrated in Figure 7.3 as a red transparent area centered on the estimated WG losses. Thus, the major factor contributing to the high uncertainty of the data is attributable to the interference occurring in the QCDs. In consequence, coupling losses actually might be as low as 4 *dB*.

7.2.3 Fabry-Pérot Cavity

The ideal photodetector absorbs 100 % of the incident light. In real devices, some of the light is reflected at the detector's facet. In the case of the measured QCDs, the interference is caused by reflections at their backside, which means that they are too transparent to absorb all the light. Hence their length of 200 μm is insufficient. To estimate an appropriate length for the QCDs, a simple model of a one-dimensional Fabry-Pérot cavity is employed. The reflectivity r_{ij} and transmissivity t_{ij} at the interface between two media i and j for light in the case of normal incidence are given by the simplified Fresnel equations:

$$\begin{aligned} r_{ij} &= \frac{n_j - n_i}{n_i + n_j}; \\ t_{ij} &= \frac{2n_i}{n_i + n_j} \end{aligned} \tag{7.2}$$

where the n stand for the complex refractive indices of the media. In the model there are three domains:

1) $x < 0 \rightarrow$ *Air*

2) $0 < x < 200\ \mu m \rightarrow$ *QCD active region*

3) $x > 200\ \mu m \rightarrow$ *Gold*

Here infinite extensions of the air and the gold domain, as well as constant refractive indices in the wavelength range of interest ($8 - 8.3\ \mu m$) are assumed. The total reflectivity r_{13} and transmissivity t_{13} of the QCD are given by:

$$\begin{aligned} r_{13} &= r_{12} + \frac{t_{12}\, t_{21}\, r_{23}\, e^{-2i\varphi}}{1 - r_{21}\, r_{23}\, e^{-2i\varphi}}; \\ t_{13} &= \frac{t_{12}\, t_{21}\, r_{23}\, e^{-2i\varphi}}{1 - r_{21}\, r_{23}\, e^{-2i\varphi}} \end{aligned} \tag{7.3}$$

with the phase factor $\varphi = ndk_0$, given by the QCD's length d, refractive index n and vacuum wavenumber $k_0 = \frac{\lambda_0}{2\pi}$. This phase factor is responsible for the observed interference. It

decreases with increasing d. The absorption A in the QCD is now obtained through:

$$A = 1 - R - T = 1 - |r_{13}|^2 - Re\left(\frac{n_3}{n_1}|t_{13}|^2\right) \tag{7.4}$$

These calculations were performed with a Python code provided by Benedikt Schwarz. To find the unknown refractive index of the QCD's active region (n_{QCD}), it is fitted until calculations reproduce the worst case of 7.8 *dB* deviation between maximum and minimum in the wavelength range of $8 - 8.3$ μm. Since the QCD's EQE is directly proportional to its absorption (Section 3.3) the maximum variation caused by interference can be expressed as:

$$\Delta_{max} = -10\log\left(\frac{A_{min}}{A_{max}}\right) \tag{7.5}$$

with the maximum and minimum absorption of the QCD. A value of $3.1425 - 0.0006j$ for n_{QCD} is found. The imaginary part is relatively low, leading to reflections at the Au on the back of the QCD that then interfere with the incoming signal. When the length of the QCD is increased, more light is absorbed before reaching the back facet, and the interference is reduced (Figure 7.6). A length of 1400 μm is required according to this simplified model to annihilate the effects of the interference, while at around 700 *nm* the value falls below 2 *dB*. For future device generations, this is an important factor to consider, since mode-hopping in the QCLs and possible differences between the n_{QCD} of individual QCDs, together with the relatively narrow interference patterns render it very hard to correct for these fringes.

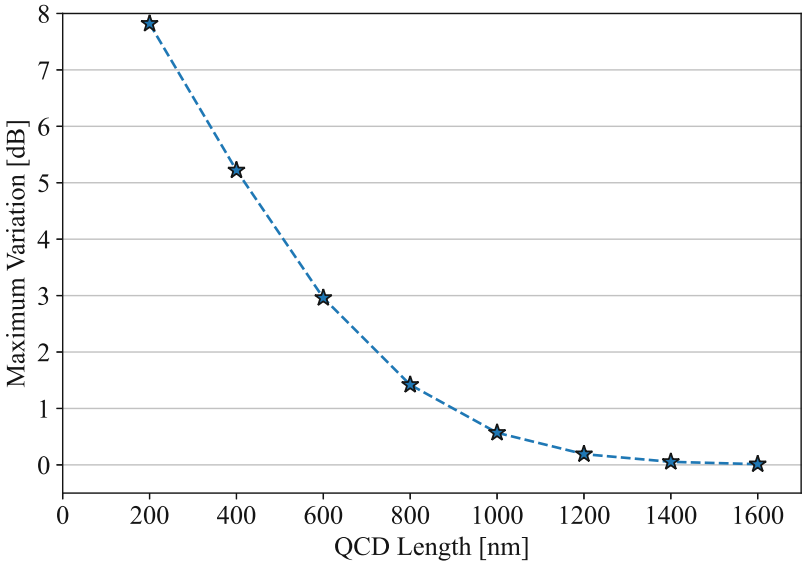

Figure 7.6: Fabry-Pérot Cavity calculation results for a cavity with n_{QCD} at different cavity lengths.

8 Signal Amplifier Characterization

For heterodyne signal detection, one of the on-chip QCLs acts as SOA. The employment of QCL material for signal amplification is commonly studied to increase the output power of a laser to Watt-level emission. This configuration is known as master-oscillator power-amplifier [58–60]. Amplifications of $12\,dB$ at at wavelength of $7.26\,\mu m$ were demonstrated [58]. To estimate the amplification reached through the SOAs in this work the signal of the EC-QCL employed for the QCD characterization is coupled through the SOAs on the chip and detected by the QCD after the plasmonic WG section. This signal is then compared to the signal obtained from a free-standing QCD. The setup for the measurements is the same as for the QCD characterization. The only difference is that the EC-QCL is aligned to the SOA's facet and that the SOA is biased through the pulse generator used for the LIV measurements. In these experiments, the supplied voltage is kept constant at values around the lasing threshold throughout one wavelength sweep ($8065 - 10000\,nm$) of the EC-QCL. The Pulser is triggered by the EC-QCL at a frequency of $4\,kHz$ and $500\,ns$ pulse width. As an example the result of one EC-QCL sweep at different SOA biases is shown in Figure 8.1. The data of the last $75\,nm$ of the spectra are substituted with a constant value corresponding to the QCD's mean signal at the given bias voltage before the EC-QCL is turned on. The SOA is the QCL of a linear device emitting at $8265\,nm$ and $8040\,nm$ at a current of $900\,mA$. The EC-QCL's signal is transmitted at appreciable strength between $8065\,nm$ up to around $8400\,nm$. The best amplification is reached between 34 and $36\,V$. From 9000 to $10000\,nm$, if at all, the EC-QCL's signal is transmitted at very high losses, as can be seen by comparing the constant signal to the last section of the spectrum representing the crosstalk signal between SOA and QCD without EC-QCL. The jump of this crosstalk between 34 and $36\,V$ suggests, that the SOA starts to

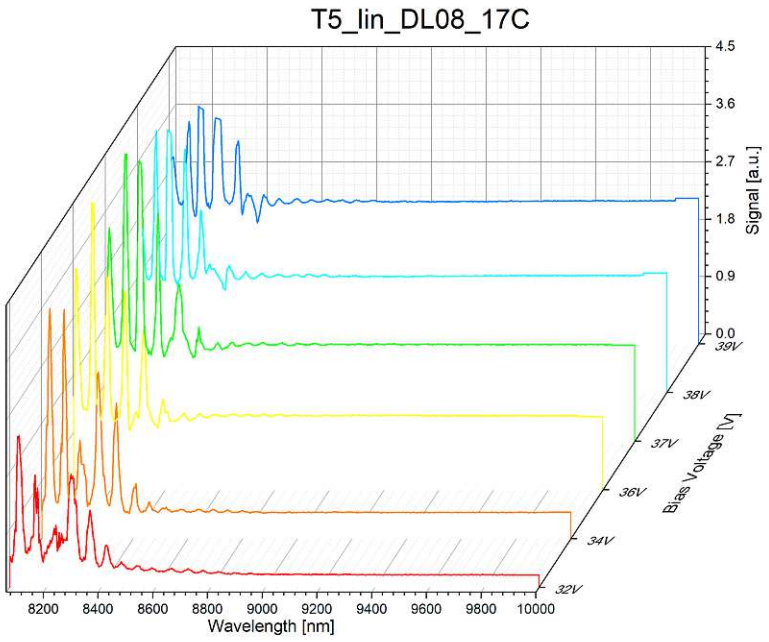

Figure 8.1: EC-QCL spectrum measured with on-chip QCD after amplification through biased SOA at different bias voltage.

lase in this range and therefore adds additionally to the baseline of the signal. Increasing the voltage beyond the lasing offset leads to strongly increasing crosstalk, but decreasing EC-QCL signal. Therefore, it is important to keep the SOA bias close to the lasing offset, to maximize the signal amplification. This point though is very sensitive to temperature, so future devices will require integrated temperature control to guarantee optimal operation. Direct comparison between the EC-QCL spectrum measured through the free-standing QCD and the signal gathered after coupling through the SOA on a linear device with a WG length of 75 *nm* is shown in Figure 8.2. The orange curve shows the acquired data of the signal coupled through the SOA after subtraction of the crosstalk baseline, to ensure a valid comparison. The signal amplified through the SOA is of similar magnitude to the free-standing QCD's signal at wavelengths between 8065 and 8350 *nm*. The losses of the linear device with a WG length of 75 μm are at least 5 *dB*, presuming the lower edge of the transparent red area in Figure 7.3. At about 8100 *nm* the SOA coupled signal is 1.8 times higher than the free-standing QCD's. This corresponds to another 5 *dB* and therefore, the total maximum gain can be estimated to reach up

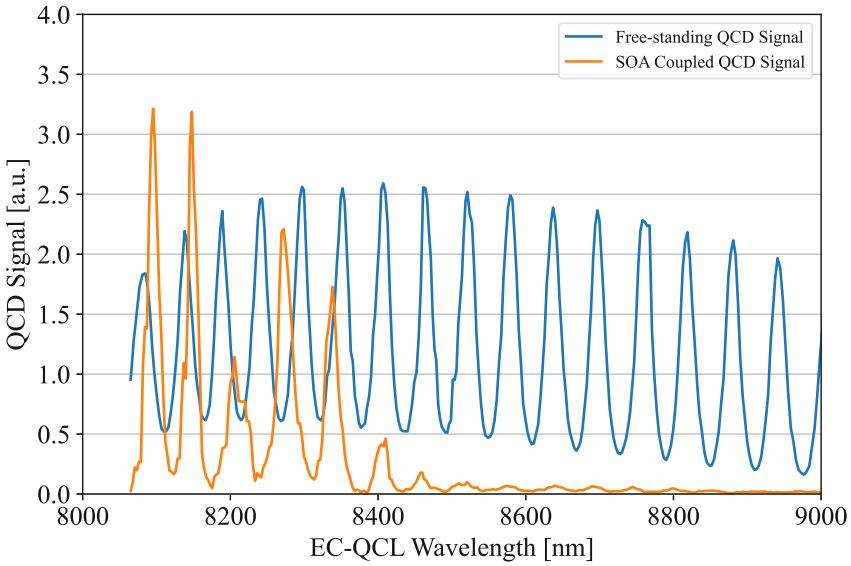

Figure 8.2: EC-QCL spectrum measured with an on-chip QCD after amplification through the biased SOA of a thin Ge linear device with a WG length of 75 μm and with a free-standing QCD.

to 10 *dB*. This data suggests that without QCD interference appreciable gain between 8065 and 8350 *nm* at the optimal bias would be possible. It has to be noted, that the lower limit is not defined, as the measurement is limited to wavelengths above 8065 *nm* by the range of the EC-QCL. Similar results are obtained from a 90° single mirror device and a 90° heterodyne device (Appendix 9.4).

9 Conclusion and Outlook

In this work, two WG geometries for beam combining in a heterodyne receiver configuration at wavelengths of $8 - 8.5$ μm were studied. Preliminary investigations employed the simulation software *COMSOL Multiphysics*. A thick WG geometry (1×2 μm) was compared to a thin WG geometry (6×0.3 μm). Simulation results showed that the thick WGs have high losses (110 *dB*/*mm*) but can redirect the propagation of SPPs even at small bending radii. The thin geometry demonstrates low losses (16 *dB*/*mm*) but SPPs propagate only in a linear direction and do not follow the WG in case of bends. The introduction of an Au-covered mirror structure is shown to successfully achieve SPP redirection of $90°$ at the cost of additional losses, around 2.2 *dB*. The results of the simulations suggest that the thick WG geometry is advantageous at WG lengths below 47 μm in a heterodyne configuration, which would require two mirrors for the thin WG geometry. In the fabrication of real devices, the thin WG design proved to be more reliable leading to a significantly higher yield of functional devices, compared to its alternative. An On-chip WG characterization, based on principles of the cut-back technique often employed for optical fibers, showed good agreement between simulation and real devices regarding WG losses. The coupling losses and the mirror losses were found to be around 7[1] and 8 *dB* respectively. Also, to the knowledge of the author, it was the first time that Au mirrors were used to redirect SPPs guided by DLSPPWGs. The high uncertainty in the data for WG characterization is mainly attributed to interference in the QCD, which acts as a Fabry-Pérot cavity. Calculations suggest that the QCD's length of 200 μm would need to be increased to 1200 μm to avoid this effect. Finally coupling experiments of an external EC-QCL indicate that the SOAs (biased QCLs with open facets) show gain at $8065 - 8400$ *nm* of up to 10 *dB*,

[1] Here the effect of the QCD interference (section 7.2.2) was not taken into account.

around the lasing threshold. Most likely this range extends further towards lower wavelengths since measurements were limited in this direction by the EC-QCLs range.

In conclusion the obtained results present a promising step towards a functional mid-infrared heterodyne receiver. The two most important improvements to be implemented in the next generation of devices are the optimization of the QCL geometry, to reach room temperature continuous wave operation, and longer QCD ridges to avoid interference patterns in the detected signal. Further AR-coatings at the SOA's and QCD's facets should be introduced to reduce reflection losses and prevent the SOA from lasing, thereby allowing higher bias voltages without contributing to the signal baseline.

References

[1] M Sadiku *et al.* “Free space optical communications: an overview”. In: *European scientific journal* 12 (2016), pp. 55–68.

[2] MA Khalighi and M Uysal. “Survey on free space optical communication: A communication theory perspective”. In: *IEEE communications surveys & tutorials* 16 (2014), pp. 2231–2258.

[3] H Henniger and O Wilfert. “An Introduction to Free-space Optical Communications.” In: *Radioengineering* 19 (2010).

[4] M Joharifar *et al.* “High-speed 9.6-μm long-wave infrared free-space transmission with a directly-modulated QCL and a fully-passive QCD”. In: *Journal of Lightwave Technology* 41 (2023), pp. 1087–1094.

[5] Accessed: 07/09/2023. url: `https://commons.wikimedia.org/wiki/File:Atmosfaerisk_spredning.png`.

[6] M David. “Plasmonic Waveguides: A New Frontier for Mid-IR Photonic Integrated Circuits”. PhD thesis. Institute of Solid State Electronics, TU Wien, Vienna, Austria, 2023.

[7] RH Ritchie. “Plasma Losses by Fast Electrons in Thin Films”. In: *Phys. Rev.* 106 (1957), pp. 874–881.

[8] CJ Powell and JB Swan. “Origin of the characteristic electron energy losses in aluminum”. In: *Physical Review* 115 (1959), p. 869.

[9] I Pockrand *et al.* “Surface plasmon spectroscopy of organic monolayer assemblies”. In: *Surface Science* 74 (1978), pp. 237–244.

[10] M Bocková *et al.* “Advances in surface plasmon resonance imaging and microscopy and their biological applications”. In: *Annual Review of Analytical Chemistry* (2019), pp. 151–176.

[11] WL Barnes *et al.* “Surface plasmon subwavelength optics”. In: *nature* 424 (2003), pp. 824–830.

[12] R Soref. “Mid-infrared photonics in silicon and germanium”. In: *Nature photonics* 4 (2010), pp. 495–497.

[13] S Law *et al.* “Towards nano-scale photonics with micro-scale photons: the opportunities and challenges of mid-infrared plasmonics”. In: *Nanophotonics* 2 (2013), pp. 103–130.

[14] W Demtröder. *Experimentalphysik 2*. Vol. 2. Springer, 2004.

[15] SA Maier *et al. Plasmonics: fundamentals and applications*. Vol. 1. Springer, 2007.

[16] E Kretschmann and H Raether. “Radiative decay of non radiative surface plasmons excited by light”. In: *Zeitschrift für Naturforschung A* 23 (1968), pp. 2135–2136.

[17] A Otto. “Excitation of nonradiative surface plasma waves in silver by the method of frustrated total reflection”. In: *Zeitschrift für Physik A Hadrons and nuclei* 216 (1968), pp. 398–410.

[18] S Park *et al.* “Resonant coupling of surface plasmons to radiation modes by use of dielectric gratings”. In: *Optics letters* 28 (2003), pp. 1870–1872.

[19] HL Offerhaus *et al.* “Creating focused plasmons by noncollinear phasematching on functional gratings”. In: *Nano letters* 5 (2005), pp. 2144–2148.

[20] C Fisher *et al.* “End-fire coupling efficiencies of surface plasmons for silver, gold, and plasmonic nitride compounds”. In: *JOSA B* 33 (2016), pp. 1044–1054.

[21] C Fisher *et al.* “Efficient end-fire coupling of surface plasmons in a metal waveguide”. In: *JOSA B* 32 (2015), pp. 412–425.

[22] JP Tetienne *et al.* “Injection of midinfrared surface plasmon polaritons with an integrated device”. In: *Applied Physics Letters* 97 (2010), p. 211110.

[23] A Edelmann *et al.* “Coupling of terahertz radiation to metallic wire using end-fire technique”. In: *Electronics letters* 49 (2013), pp. 884–886.

[24] M David *et al.* “Octave-spanning low-loss mid-IR waveguides based on semiconductor-loaded plasmonics”. In: *Optics Express* 29 (2021), pp. 43567–43579.

[25] S Hayashi and T Okamoto. “Plasmonics: visit the past to know the future”. In: *Journal of Physics D: Applied Physics* 45 (2012), p. 433001.

[26] S Bühler-Paschen, H Michor, and M Reissner. *Festkörperphysik I*. TU Wien. 2018.

[27] R Pecharromán-Gallego. “An Overview on Quantum Cascade Lasers: Origins and Development”. In: *Quantum Cascade Lasers*. Ed. by Vasilios N. Stavrou. 2017. Chap. 1. doi: 10.5772/65003. url: https://doi.org/10.5772/65003.

[28] A Harrer. “Quantum Cascade Intersubband Devices for Mid-Infrared Sensing”. PhD thesis. Institute of Solid State Electronics, TU Wien, Vienna, Austria, 2017. Doctoral dissertation.

[29] B Hinkov. “Monolithic integration of mid-infrared photonics”. PhD thesis. ETH Zurich, Zurich, Swizerland, 2015. Doctoral dissertation.

[30] B Schwarz. “Monolithic integration of mid-infrared photonics”. PhD thesis. Institute of Solid State Electronics, TU Wien, Vienna, Austria, 2015. Doctoral dissertation.

[31] RF Kazarinov and A Suris. “Possibility of the amplification of electromagnetic waves in a semiconductor with a superlattice”. In: *Sov. phys. semicond* 5 (1971), p. 207.

[32] J Faist *et al.* “Quantum cascade laser”. In: *Science* 264 (1994), pp. 553–556.

[33] M Wienold *et al.* “Evidence for frequency comb emission from a Fabry-Pérot terahertz quantum-cascade laser”. In: *Optics Express* 22.25 (2014), pp. 30410–30424.

[34] BG Lee *et al.* “DFB quantum cascade laser arrays”. In: *IEEE Journal of Quantum Electronics* 45.5 (2009), pp. 554–565.

[35] CK Akhgar *et al.* “The next generation of IR spectroscopy: EC-QCL-based mid-IR transmission spectroscopy of proteins with balanced detection”. In: *Analytical Chemistry* 92 (2020), pp. 9901–9907.

[36] M S Vitiello *et al.* “Quantum cascade lasers: 20 years of challenges”. In: *Optics express* 23 (2015), pp. 5167–5182.

[37] B Hinkov *et al.* “A mid-infrared lab-on-a-chip for dynamic reaction monitoring”. In: *Nature communications* 13 (2022), p. 4753.

[38] B Schwarz *et al.* “High performance bi-functional quantum cascade laser and detector”. In: *Applied Physics Letters* 107 (2015).

[39] G Bastard. “Wave mechanics applied to semiconductor heterostructures”. In: (1990).

[40] A Delga. “Quantum cascade detectors: A review”. In: *Mid-infrared Optoelectronics* (2020), pp. 337–377.

[41] D Hofstetter, M Beck, and J Faist. “Quantum-cascade-laser structures as photodetectors”. In: *Applied Physics Letters* 81 (2002), pp. 2683–2685.

[42] G Marschick *et al.* “High-responsivity operation of quantum cascade detectors at 9 μm”. In: *Optics Express* 30 (2022), pp. 40188–40195.

[43] B Schwarz *et al.* “The limit of quantum cascade detectors: A single period device”. In: *Applied Physics Letters* 111 (2017).

[44] Y Zou *et al.* “Monolithically integrated quantum cascade lasers, detectors and dielectric waveguides at 9.5 μm for far-infrared lab-on-chip chemical sensing”. In: *2015 Conference on Lasers and Electro-Optics (CLEO)*. IEEE. 2015, pp. 1–2.

[45] B Schwarz. “Monolithic integration of mid-infrared photonics”. Doctoral dissertation. Wien, 2015.

[46] D Palaferri *et al.* “Room-temperature nine-μm-wavelength photodetectors and GHz-frequency heterodyne receivers”. In: *Nature* 556 (2018), pp. 85–88.

[47] MC Teich. “Infrared heterodyne detection”. In: *Proceedings of the IEEE* 56 (1968), pp. 37–46.

[48] J Griffith. “Laser heterodyne spectroscopy”. In: *Philosophical Transactions of the Royal Society of London. Series A, Mathematical and Physical Sciences* 307 (1982), pp. 563–571.

[49] AT Forrester. “Photoelectric mixing as a spectroscopic tool”. In: *JOSA* 51 (1961), pp. 253–259.

[50] TG Phillips and J Keene. “Submillimeter astronomy (heterodyne spectroscopy)”. In: *Proceedings of the IEEE* 80 (1992), pp. 1662–1678.

[51] F Gibert *et al.* “Two-micrometer heterodyne differential absorption lidar measurements of the atmospheric CO 2 mixing ratio in the boundary layer”. In: *Applied optics* 45 (2006), pp. 4448–4458.

[52] RF Lucy *et al.* “Optical superheterodyne receiver”. In: *Applied optics* 6 (1967), pp. 1333–1342.

[53] OE DeLange. “Optical heterodyne detection”. In: *IEEE spectrum* 5 (1968), pp. 77–85.

[54] BM Oliver. “Thermal and quantum noise”. In: *Proceedings of the IEEE* 53 (1965), pp. 436–454.

[55] *Wave Optics Module*. Accessed: 2023-09-13. 2023. url: `https://www.comsol.com/wave-optics-module`.

[56] *multyphisics CYCLOPEDIA: The Finite Element Method (FEM)*. Accessed: 2023-08-14. 2016. url: `https://www.comsol.de/multiphysics/finite-element-method`.

[57] KI Martin, WA Clarkson, and DC Hanna. “Self-suppression of axial mode hopping by intracavity second-harmonic generation”. In: *Optics letters* 22 (1997), pp. 375–377.

[58] S Menzel *et al.* “Quantum cascade laser master-oscillator power-amplifier with 1.5 W output power at 300 K”. In: *Optics express* 19 (2011), pp. 16229–16235.

[59] B Hinkov *et al.* “Quantum cascade laser in a master oscillator power amplifier configuration with Watt-level optical output power”. In: *Optics express* 21 (2013), pp. 19180–19186.

[60] P Rauter *et al.* “Master-oscillator power-amplifier quantum cascade laser array”. In: *Applied Physics Letters* 101 (2012).

Acknowledgements

Here I want to write a few lines to express my gratitude toward all the wonderful people who supported me throughout my work on this thesis. A special thanks goes to Mauro, who not only lured me to join the great research group I worked with but also introduced me to the world of COMSOL simulations. Thanks to Borislav, for assembling such an amazing bunch of people, for offering me this interesting project, and for your supervision with all the support a master's student can wish for. Thanks to Georg for the great processing of the devices, the patience with the many suggestions regarding design improvement, which you managed to implement wonderfully, and the great ice hockey games I could watch. Thanks to Dominik for the vital support in the Lab, fighting software and hardware issues in the pursuit of gathering good data. Thanks to Elena for the moral support, always bringing joy to the office and the lab, and starting great lunch discussions over the most important issues in the universe and beyond. Thanks to Stefi for sharing the quiet office hours in the morning and for performing the ellipsometry measurements at such short notice. Thanks to Miki for the assistance with the FTIR and your good sense of sarcasm, which I might actually miss. Thanks also to the broader optoelectronic materials group for their help and their great company after long office/lab hours. Here I want to mention Rolf, Andi, Flo, Kristina, Daniele, and Anna. Finally, I want to thank my family and my friends outside of university for their support during this challenging time.

Without the people mentioned above I couldn't have accomplished this work. Thank you!

Appendix:
Additional Plots and Tables

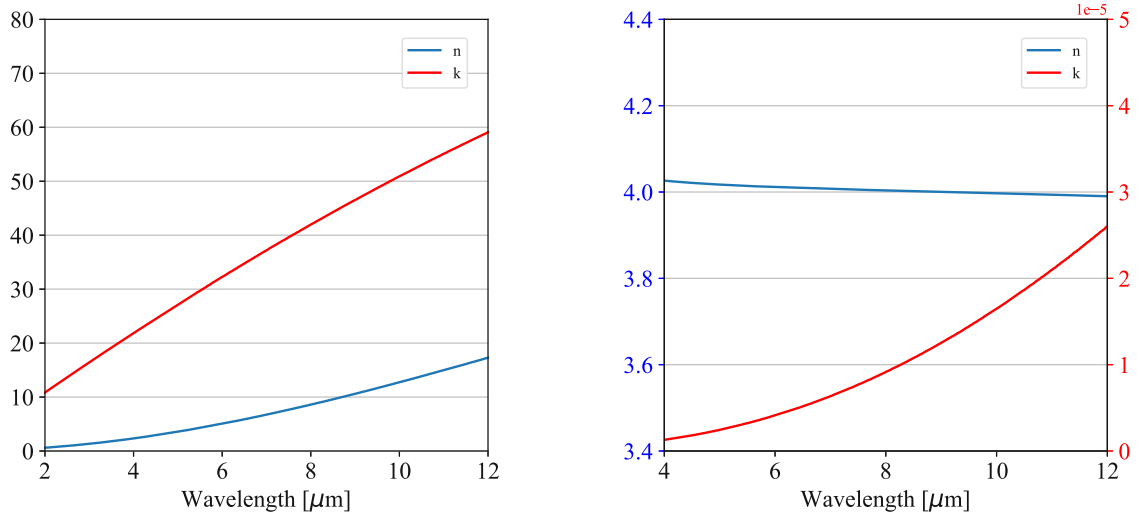

(a) **(b)**

Figure 9.1: Real n and imaginary k parts of the refractive index of **(a)** Gold and **(b)** Germanium obtained through ellipsometry measurements performed at the *Central European Institute of Technology* at Brno. Material parameters for WG simulations were extracted from this data.

Configuration	QCL Length [μm]	QCD Length [μm]	Mirror Length [μm]	WG Length / Gap Size [μm]
Linear (No WG)	3500	194	x	1 / 2 / 3 / 4
Linear	3500	194	x	25 / 50 / 75 / 100 / 150
90° Single Mirror	3740	200	50	57.5 / 177.5
90° HD	3.500/3.860	200	46 / 30	93.5 / 153.5
100° HD	3.500/3.790	200	48 / 30	106.6 / 154.2

Table 9.1: QCLD device parameters of the 2nd Generation Thin Ge WG designs. The width of the QCL and QCD ridges is 14 μm and the waveguide width is 6 μm in all devices. The gap size between the mirrors and Ge WGs does not exceed 2μm.

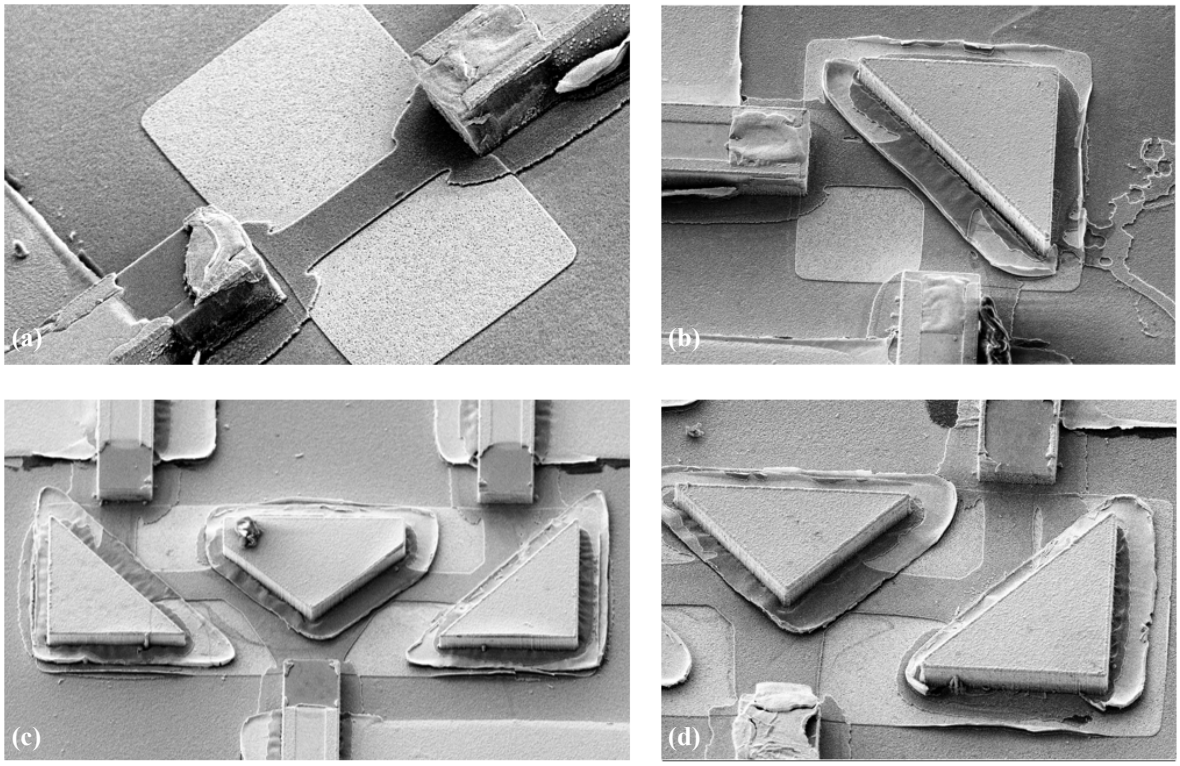

Figure 9.2: 1st Generation of thin Ge devices. **(a)** Linear design. Ge residuals are splashed around the QCLD ridges. Some devices work, but the performance is low. **(b)** 90° single mirror device. **(c)** 100° heterodyne structure. **(d)** 90° heterodyne structure. In all of the devices with mirrors shown in the Figure, which represent the majority of the 1st generation, the gold covering the triangular shaped mirror structures detached, interrupting the Ge WGs and disabling the devices.

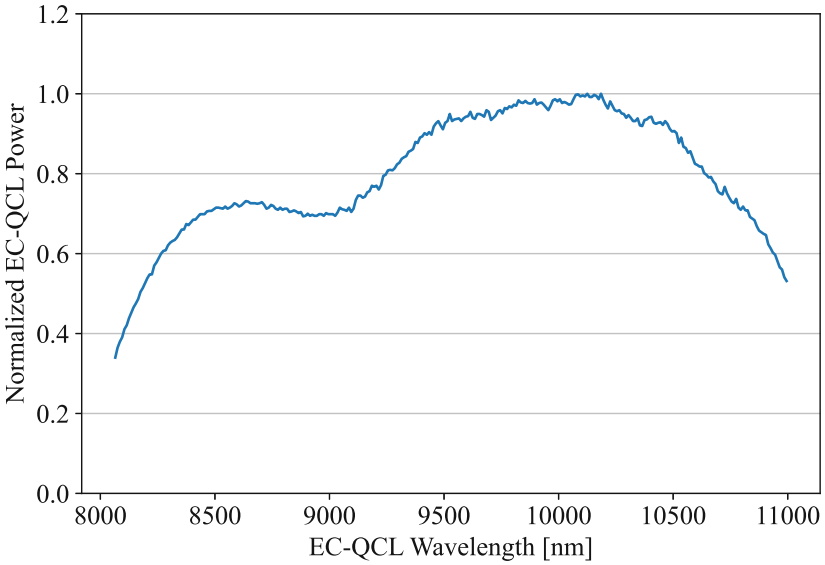

Figure 9.3: Normalized EC-QCL spectrum obtained through power sensor (Thorlabs S401C) measurements. This curve is used for the calibration of data gathered from EC-QCL wavelength sweeps.

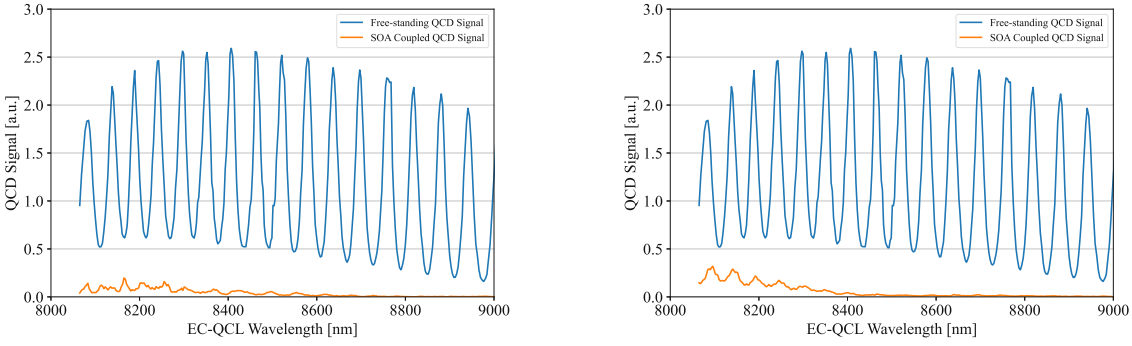

(a) **(b)**

Figure 9.4: EC-QCL coupled through biased SOA of **(a)** a 177 *nm* (15 *dB* losses) WG single mirror device and **(b)** a 93.5 *nm* WG 90° heterodyne detector (25 *dB* losses) compared with the signal of a free-standing QCD. The electric crosstalk is subtracted from the SOA signals.